TECHNISCHE UNIVERSITÄT WIEN
Vienna | Austria

DIPLOMARBEIT

Magnetic correlation length at quantum criticality: The role of Fermi surface geometries

zur Erlangung des akademischen Grades

Diplom-Ingenieur

im Rahmen des Studiums

Technische Physik

eingereicht von

Dominik Robert Fus, BSc
Matrikelnummer: 11805818

ausgeführt am Institut für Festkörperphysik
der Fakultät für Physik der Technischen Universität Wien

Betreuer: Associate Prof. Dr. Alessandro Toschi
Co-Betreuer: Dr. Thomas Schäfer (MPI-FKF Stuttgart)

Wien, August 22, 2024

(Unterschrift Verfasser) (Unterschrift Betreuer)

Contents

Abstract

Strongly correlated electron systems exhibit some of the most fascinating phenomena of condensed matter physics. Beyond the famous example of the Mott-Hubbard metal-to-insulator transition and the occurrence of classical phase transitions to magnetic and charge ordered states as well as superconductivity, several quantum phase transitions can be found in the phase diagrams of strongly correlated systems. These transitions are quite intriguing, because they occur at zero temperature, where quantum fluctuations dominate the physics in contrast to their classical, thermal counterparts. The study of quantum phase transitions does not represent, in any case, a mere academic exercise, as their occurrence affect broad finite-temperature sectors of the phase diagrams of correlated materials. Their theoretical description for correlated electron systems faces big challenges, both analytical and numerical, so that a comprehensive theory could not be established hitherto. This master thesis aims at improving our fundamental theoretical understanding of quantum phase transitions in correlated bulk metals by performing thorough numerical and analytical investigations. In particular, for the former we resort to the dynamical mean-field theory (DMFT), which includes purely local temporal correlations, while analytical derivations will mostly exploit the random phase approximation (RPA). These quantum many-body methods are applied to one of the most fundamental model systems in condensed matter physics, the Hubbard model on three dimensional lattices. By means of DMFT and RPA, the magnetic susceptibility and the corresponding correlation length in all the relevant regimes around a magnetic quantum critical point in the Hubbard model are determined, clarifying the previously not understood behavior of the latter quantity. This provides further evidence for a significant violation of the predictions of the conventional Hertz-Millis-Moriya theory, triggered by specific geometrical properties of the underlying Fermi surfaces, and for their effects on the whole phase-diagram around the corresponding magnetic quantum critical points.

Deutsche Kurzfassung

Stark korrelierte Elektronensysteme zeigen einige der faszinierendsten Phänomene der Festkörperphysik. Jenseits bekannter Beispiele, wie dem Mott-Hubbard-Übergang vom Metall zum Isolator, dem Auftreten klassischer Phasenübergänge zu magnetischen und ladungsgeordneten Zuständen, sowie der Supraleitung, sind in den Phasendiagrammen stark korrelierter Systeme verschiedene Quantenphasenübergänge zu finden. Diese Übergänge sind besonders interessant, da sie am absoluten Nullpunkt auftreten. Im Gegensatz zu ihren klassischen, thermischen Gegenstücken dominieren hier Quantenfluktuationen. Die Untersuchung von Quantenphasenübergängen stellt keineswegs eine rein akademische Übung dar, da ihr Auftreten weite Temperaturbereiche der Phasendiagramme korrelierter Materialien beeinflusst. Ihre theoretische Beschreibung in korrelierten Elektronensystemen stellt sowohl analytisch als auch numerisch große Herausforderungen dar, sodass eine umfassende Theorie bisher nicht entwickelt werden konnte. Diese Diplomarbeit zielt darauf ab, unser grundlegendes theoretisches Verständnis von Quantenphasenübergängen in korrelierten Massenmetallen durch gründliche numerische und analytische Untersuchungen zu verbessern. Für die numerischen Untersuchungen greifen wir insbesondere auf die Dynamische Molekularfeldtheorie (DMFT) zurück, die rein lokale zeitliche Korrelationen berücksichtigt, während die analytischen Ableitungen größtenteils die Random-Phase-Approximation (RPA) nutzen. Diese quantenmechanischen Vielteilchenmethoden werden auf eines der grundlegendsten Modellsysteme der Festkörperphysik angewendet, das Hubbard-Modell in dreidimensionalen Gittern. Durch DMFT und RPA werden die magnetische Suszeptibilität und die dazugehörige Korrelationslänge in allen relevanten Bereichen um einen magnetischen Quantenkritischen Punkt im Hubbard-Modell bestimmt, wodurch das bisher nicht verstandene Verhalten letzter Größe geklärt wird. Dies liefert weitere Hinweise auf eine signifikante Verletzung der Vorhersagen der konventionellen Hertz-Millis-Moriya-Theorie, ausgelöst durch spezifische geometrische Eigenschaften der zugrunde liegenden Fermi-Flächen, und auf deren Auswirkungen auf das gesamte Phasendiagramm um die entsprechenden magnetischen quantenkritischen Punkte.

Dedication and Acknowledgements

First of all I would like to say “grazie” to my supervisor, Professor Alessandro Toschi. His passion for physics has been constantly motivating me throughout my time at his group. Professor Toschi’s guidance and engaging discussions have greatly enriched my understanding of the subject.

I would also like to thank my co-supervisor, Dr. Thomas Schäfer. His valuable advice since the beginning of my studies has been most valuable to my development at our beloved TU Wien. I am especially grateful for the opportunity and invitations he provided to collaborate in Stuttgart with him and his great students.

Thank you both for your support and mentorship.

I am also grateful to the members of our group and those in Stuttgart who have been consistently supportive and open to discussions: Herbert Eßl, Emin Moghadas, Matthias Reitner, and Michael Meixner. A special thanks goes to my additional supervisors, Severino Adler and Mário Malcolms de Oliveira, for their great assistance with the technical aspects of this thesis.

I would also like to extend my thanks to Karsten Held, Andrey Katanin, Georg Rohringer, and Giorgio Sangiovanni for their valuable discussions that significantly advanced this project. Additionally, I am grateful to the Flatiron Institute in New York City for their warm hospitality and for providing me with the opportunity to present this work for the first time.

Additionally, I want to thank the wonderful people at the student office who became like a second family to me: Alena (aka Higgs), Conni (aka Mei), Daniel (aka Killian), Florian (aka Brillouin), Katja (aka Tito), Patrick (aka Mystery), Samuel (aka Ingrid), and Selina (aka Roan). You made the past two years incredibly enjoyable and fun.

Zuletzt möchte ich mich bei meinen Eltern und meiner Schwester bedanken. Danke, dass ihr immer an mich glaubt und mich auf all meinen Wegen begleitet.

Finally, I acknowledge financial support from the Austrian Science Fund (FWF) through grants 10.55776/I5868 (Project P1 of the research unit QUAST, FOR5249, of the German Research Foundation, DFG) and 10.55776/I5487. Most of the numerical calculations presented in this thesis were performed on the Vienna Scientific Cluster (VSC).

Chapter 1

Introduction

"Only the quality has future"

—*Mirco Gozzoli*

In our everyday lives, we are constantly surrounded by substances in various states of matter. A phase is a state in which the macroscopic physical properties are uniform on certain scales. Common examples include ice, liquid water, and water vapor, each representing a distinct aggregation state of the molecule H_2O. The macroscopic scale we observe in our daily life is evidently different from the microscopic scale of the atomic world, and the attempt of linking the microscopic processes to the macroscopic phenomena indeed one of the main goals of statistical mechanics.

A phase is characterized by a thermodynamic function, e.g. the (Gibbs) free energy, which depends on macroscopic parameters such as temperature and (pressure) volume. The values of these parameters typically determine the phase of a substance. A phase diagram, like the one shown in Fig. 1.1, represents these variables on its axes indicating the corresponding phase for each point. It may include phase-boundaries, critical points, triple points, and more. In particular, we recall that, a phase boundary separates different phases, and changing a parameter like temperature across this boundary induces a phase transition, such as, e.g., melting. In the presence of a critical point at the end of a phase boundary the two phases become indistinguishable, exhibiting unusual behavior that is explained by the theory of critical phenomena [1].

Phases can be characterized by various physical quantities. In the most common cases, in the low temperature regime, a significant one is represented by the order parameter. This is often linked to the spontaneous breaking of one of the underlying physical symmetries of the system. The order parameter, which can be an observable associated to the asymmetry properties of the broken symmetry phase, is then non-zero in the ordered phase (lower-symmetry state) and vanishes in the disordered phase (symmetric phase) [1].

In magnetic materials, the order parameter is characterized by the magnetization, where microscopic electronic spins sum up to the macroscopic observed magnetism. The spontaneously

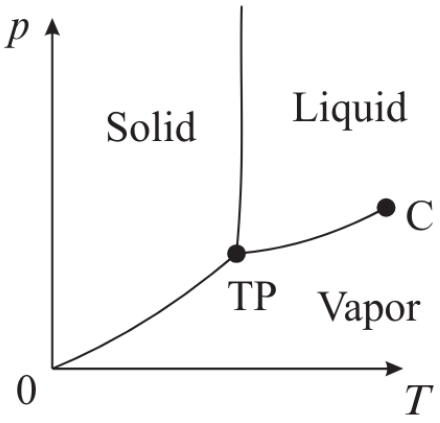

Figure 1.1: The phase of a typical substance (taken from [1]), which is determined by the values of the control parameters (here: temperature T and pressure p). C is indicating the critical point, while TP is the triple point, where all three phases meet.

broken symmetry can be associated with the orientation of the spins. Determining the order parameter is not always that straightforward. Some phases do not even have a local order parameter to characterize them. Moreover, certain order parameters couple to external physical probes (e.g., magnetization couples to an externally applied magnetic field), while others do not (e.g., the phase of the macroscopic wave function, which is the superconducting order parameter, does not couple to any physical external probe) [1].

Phase transitions can be defined by an abrupt, non-analytical behavior of the function describing the thermodynamic properties of the system. Two common definitions are found in the literature. After discovering a surprising new phase transition in liquid helium in 1932, P. Ehrenfest [2] proposed that an n- order phase transition is characterized by a discontinuity in the n-th order derivative of the free energy with respect to any of its arguments. One can further schematically divide phase transitions into those generating latent heat and those not generating latent heat. It has subsequently been observed that, in addition to discontinuities, divergences can also appear at phase transitions [3].

A more modern definition, elaborated in various textbooks [4, 5], extends Ehrenfest's definition. A first-order transition is described by a discontinuity in the derivative of an appropriate thermodynamic potential. A second-order phase transition (also called a continuous phase transition) is continuous in its first derivative but exhibits discontinuous or divergent behavior in its second derivatives, with no latent heat involved. In Fig. 1.2 we showcase the behaviour, by the thermodynamic derivatives of the free energy F, such as in the entropy $S = -\left(\partial F/\partial T\right)_V$ and the specific heat $C_V = -T\left(\partial^2 F/\partial T^2\right)$ [6].

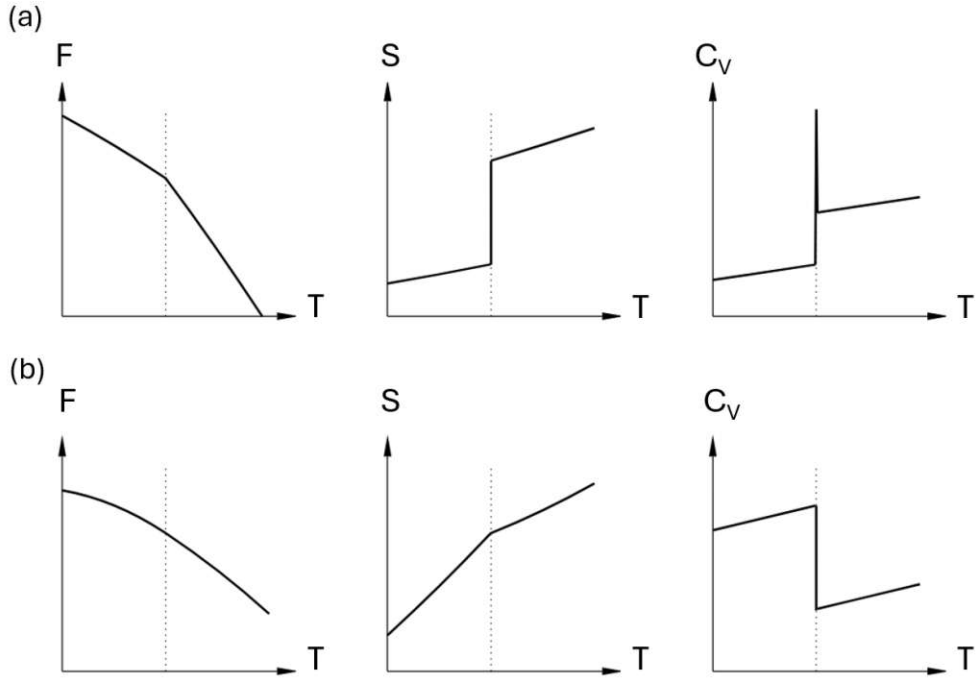

Figure 1.2: Classifications of phase transitions (readapted from [6]): Free energy F and its derivatives. (a) First-order phase transition characterized by a discontinuity in the Entropy $S = -(\partial F/\partial T)_V$ and a divergence in the specific heat $C_V = -T(\partial^2 F/\partial T^2)$. (b) Second-order phase transition with a kink in S and jump in C_V. The critical temperature T_c is indicated by the dotted line.

1.1 Quantum Phase Transitions

Phase transitions occurring at temperature $T = 0$ driven by a non-thermal control parameter (such as pressure, magnetic field, or chemical composition) are known as quantum phase transitions (QPTs). The specific point along the $T = 0$ axis where the transition occurs is called a quantum critical point (QCP). The QCP is characterized by the non-analytic behavior of the ground-state energy as a function of the control parameter. QPTs are driven by "quantum fluctuations" since thermal fluctuations at zero temperature are obviously absent. We state that at zero temperature, a quantum system is described by a single phase-coherent (many-body) wave-function. Therefore, "fluctuations" refer here to deviations from a reference state (e.g., an ordered magnet). While $T = 0$ is experimentally inaccessible, the interest lies in the impact of the quantum phase transitions (and of their associated QCPs) on finite temperature regimes [7]. To gain a first insight into the influence of quantum criticality at finite temperatures, we consider a schematic quantum critical phase diagram in Fig. 1.3.

At zero temperature, the transition between the ordered and quantum disordered ground states occurs with the change of the non-thermal order parameter at the QCP. However, there is a finite temperature region above the QCP where quantum fluctuations dominate over thermal fluctuations. This often "funnel"-shaped region in the phase diagram is referred to as quantum critical, where the most direct influence of a QCP is visible at finite temperatures. Of course, at

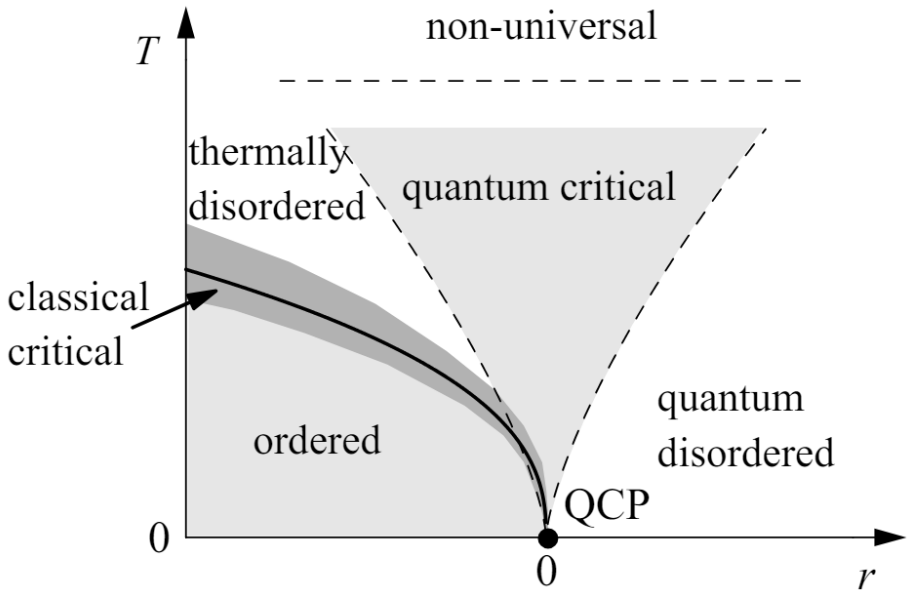

Figure 1.3: Schematic phase diagram of a QPT (taken from [8]). Tuning a non-thermal order parameter r at $T = 0$ the systems ground state changes from an ordered to a quantum disordered state, with the quantum critical point at the transition. The quantum critical funnel defines the region where quantum fluctuations dominate over thermal fluctuations.

finite T, the ordered state can also transition to a thermally disordered state driven by thermal fluctuations in the manner of a classical phase transition [9]. For a magnetic system, tuning of the corresponding transition temperature can be achieved by electron or hole doping. The ordered state could be e.g. commensurate/incommensurate (anti)ferromagnetic (AF, i-AF), with a phase transition to a paramagnetic (PM) (disordered) state. In these cases, the phase transitions are characterized by the local magnetization as an order parameter.

Thermodynamically stable phases of correlated metals usually exhibit conventional quasiparticle (QP) excitations, meaning that quantum numbers, identifiable through sharp peaks in spectral functions, can be assigned to the QPs. In Fermi liquid systems, these could be particle-hole excitations, whereas for ordered magnetic states, spin waves build the quasiparticle spectrum. In such situations, these quasiparticle states can be described in terms of their low-temperature thermodynamics as thermal occupations, with specific physical hallmarks, such as, e.g., the textbook linear-in-temperature specific heat in a Fermi liquid [7].

However, elementary excitations of the quantum critical ground state often cannot be characterized by quasiparticles, displaying a critical continuum of excitations. This critical continuum will be excited upon rising temperature in the parameter regime right above the QCP, leading to thermodynamic observables exhibiting power-law behavior as a function of temperature, characterized by non-trivial exponents. The ground state at the QCP is sometimes regarded as a "novel state of matter" characterized by these power laws, which are the experimentally observable signatures of quantum criticality [7, 9, 10].

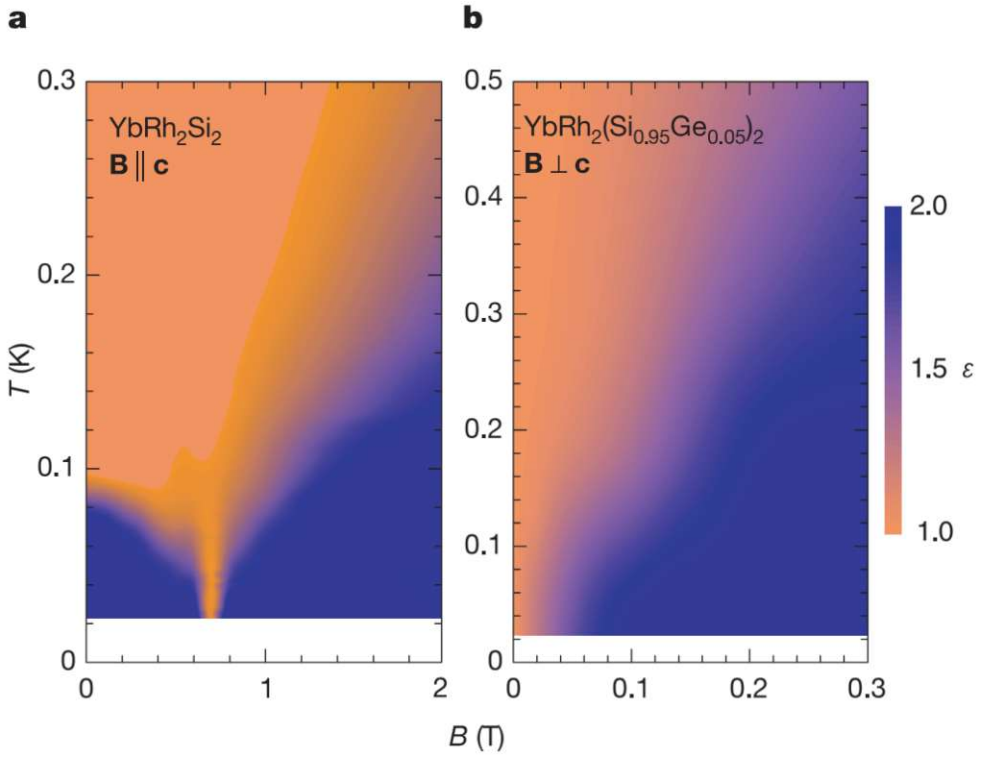

Figure 1.4: Quantum critical phase diagram of $YbRh_2(Si_{1-x}Ge_x)_2$ (taken from [11]) with the exponents of the resistivity $\delta\rho = \rho(T) - \rho_0 \propto T^\epsilon$ setting the colour scale. For the undoped compound (a), the critical magnetic field B_c is 0.66 T with a residual resistivity of 1 $\mu\Omega$·cm, while the doped compound (b) has a significantly lower B_c of 0.027 T and a higher residual resistivity of 5 $\mu\Omega$·cm. Both samples transition from a non-Fermi liquid (NFL, orange region with $\epsilon = 1$) to a heavy Fermi liquid (LFL, blue ares, resistivity scales with T^2) state at lower temperatures, but the substitution with Ge shifts the pressure needed to reach the antiferromagnetic ordering and affects the critical temperature T_N and volume expansion.

In Fig. 1.4, quantum critical phase diagrams from the compound $YbRh_2(Si_{1-x}Ge_x)_2$ are shown, with a magnetic field B as a tuning parameter. The temperature dependence of the resistivity, more precisely the exponent controlling its low-temperature power low, distinguishes the phases shown in Fig. 1.4. There, the values of the resistivity exponents are displayed in a colour scale, indicating a linear in T behaviour in the quantum critical (non-Fermi liquid) region (orange), whereas the resistivity scales as T^2 in the Fermi liquid phase (blue). The quantum critical funnel appearing in the left panel of Fig. 1.4 exhibits approximately a square root-like shape in the T–B phase diagram, or, in any case a sublinear B dependence of its borders, which is a commonly observed behavior.

Quantum critical phenomena are widely studied in condensed matter physics, their underlying relation with superconductivity being one of the "holy grails" of the field. As mentioned before, the appearance of a QCP in a phase diagram results in an unusual excitation spectrum at finite temperatures. This feature can in turn, cause non-Fermi liquid behaviors, such as linear in temperature resistivity for optimally doped cuprates [12, 13] as well as Fe-based superconductors[14],

in contrast to the $\rho \propto T^2$ behavior typical of a Fermi liquid. Consequently, some theoretical frameworks for explaining high-temperature superconductors propose that a QCP might be "hidden" beneath the superconducting dome, driving the formation of the different unconventional phases observed at finite temperatures [15].

1.2 Theoretical Descriptions

In 1937, Lev Landau established a theory based on the concept of a local order parameter ϕ in his work *On the Theory of Phase Transitions* [16]. Near critical points, the order parameter needs to be small, consistent with Landau's description of ϕ. To derive thermodynamic properties, a thermodynamic potential f as a function of the order parameter was considered to address the challenge of the previously discussed non-analytical behavior characterizing second-order phase transitions. Generally, the form of f is not known. However, near criticality, where ϕ is small, it can be expanded in a Taylor series in ϕ, if one assumes its analytically:

$$f(T, H, \phi) = f_n + f_0 \left(\frac{a}{2}\phi^2 + \frac{b}{4}\phi^4 + \cdots - h\phi \right), \tag{1.1}$$

with an external field $h = \frac{H}{f_0}$ coupling to the order parameter, and a weakly temperature-dependent term f_n, which is usually neglected. The coefficients a and b are assumed to be smooth functions of external parameters, in order to keep the problem's symmetries. The minima of the function f can be determined by the condition $\frac{\partial f}{\partial \phi} = 0$, which determines the expected value for the order parameter. Therefore the coefficient b needs to be a positive constant (otherwise $|\phi|$ would tend to infinity) and $a = a(T)$ has to change sign from positive to negative at the phase transition otherwise $|\phi|$ would always vanish. With the phase transition at $T = T_c$, it is convenient to introduce the reduced temperature $t \equiv \frac{T - T_c}{T_c}$ and identify $a(T) = \alpha \frac{T - T_c}{T_c} = \alpha t$ [7].

In extending Landau's concepts to the Ginzburg-Landau (GL) theory, the order parameter ϕ acquires an explicit spatial dependence $\phi(\vec{r})$. The Landau function can be thus generalized to the Landau-Ginzburg functional, which reads [7]:

$$f(T, H, \phi(\vec{r})) = \int d^d r \quad f_n + f_0 \left(\frac{a}{2}\phi(\vec{r})^2 + \frac{b}{4}\phi(\vec{r})^4 + \xi_0^2 (\nabla_{\vec{r}}\phi(\vec{r}))^2 - h\phi(\vec{r}) \right), \tag{1.2}$$

where an additional term appears, arising from an expansion in powers and gradients of $\phi(\vec{r})$ with the lowest allowed power by the symmetry of the problem. The Ginzburg-Landau theory is often used in the field of superconductivity due to its applicability for describing the superconducting condensate (which becomes inhomogeneous in the presence of an external magnetic field or electrical currents) with a complex scalar field ϕ [7, 17].

Minimizing the function Eq. (1.1), or, equivalently, the functional Eq. (1.2) in the absence of

a magnetic field yields the value of the order parameter ϕ as a function of the temperature T. While the order parameter is zero at $T > T_c$, at $T < T_c$ we get:

$$\phi = \pm\sqrt{\frac{\alpha}{b}(-t)} \propto -t^{0.5}. \tag{1.3}$$

In the next step, by calculating the response function $\chi := \left.\frac{\partial\phi}{\partial h}\right|_{h\to 0}$, one can observe how the susceptibility behaves at the phase transition:

$$\chi(T) \propto \frac{1}{|t|} \propto |t|^{-1}, \tag{1.4}$$

featuring a divergent behavior defined by the (mean-field, s. next subsection), critical exponent γ_{cl}, i.e. $\chi(T) \propto |t|^{-\gamma_{cl}}$, with $\gamma_{cl} = 1$. Moreover, the GL theory is well-suited to calculate spatial correlations of the order parameter ϕ. Introducing the correlation function [7]:

$$G(\vec{r},\vec{r}\,') = \langle\phi(\vec{r})\phi(\vec{r}\,')\rangle - \langle\phi(\vec{r})\rangle\langle\phi(\vec{r}\,')\rangle = \langle\phi(\vec{r})\phi(\vec{r}\,')\rangle - \phi_0^2, \tag{1.5}$$

with ϕ_0 being the spatially homogeneous equilibrium value of ϕ. Therefore, in the ordered phase where long-range order exists [7]:

$$\lim_{|\vec{r}-\vec{r}\,'|\to\infty} \langle\phi(\vec{r})\phi(\vec{r}\,')\rangle = \phi_0^2 > 0. \tag{1.6}$$

Here, $G(\vec{r},\vec{r}\,')$ describes the fluctuations around ϕ_0. Following the derivation performed in [18], after some steps the Fourier transformed correlation function reads:

$$G(k) = \langle\delta\phi(\vec{k})\,\delta\phi(-\vec{k})\rangle = \frac{kT}{f_0(A+\xi_0^2k^2)}, \tag{1.7}$$

where $\delta\phi$ is the deviation of the order parameter from its equilibrium value ϕ_0 and $A = \alpha t + 3b\phi_0^2$ ($a = \alpha t$)). Performing a Fourier transformation back to real space, we obtain the correlation function depending on the dimensionality d, which in the limit of large $r = |\vec{r}-\vec{r}\,'|$) reads [7]:

$$G(r) \propto \frac{e^{-r/\xi(T)}}{r^{(d-1)/2}}\xi^{(3-d)/2}. \tag{1.8}$$

Hence, the correspondingly defined correlation length ξ in the GL theory depends on the reduced temperature t as

$$\xi(T) \propto \frac{1}{\sqrt{|t|}} \propto t^{-0.5}, \tag{1.9}$$

corresponding to a (mean-field) critical exponent $\nu_{cl} = \frac{1}{2}$. Here we see that, as the critical point is approached, ξ diverges, which can be heuristically associated with the formation of locally ordered fluctuating regions, whose size increase as $T \to T_c$. Observations of a slowly varying order parameter in space near phase transitions a posteriori justifies the gradient expansion in Ginzburg-Landau theory [7, 9].

In summary, we introduced the Landau and Ginzburg-Landau functionals, which allows to compute the temperature dependence of the order parameter, susceptibility, and correlation length in a static mean-field framework. A more general approach would allow the order parameter to fluctuate in space and time. In the GL formulation above, however, ϕ was fixed by solving the minimization problem, thereby essentially neglecting the corresponding fluctuations. This is what renders the Landau theory a mean-field(-type) approximation.

Now a question naturally arises: To what extent is it valid to neglect fluctuations? While, in general, one would expect that fluctuations can be rigorously neglected only for $d \to \infty$, the divergence of the correlation length for $T \to T_c$ allows for a different, somewhat less strict, criterion: The so-called Ginzburg criterion [1, 7] states that fluctuations become important upon approaching criticality in dimensions $d < 4$, but are irrelevant for $d > 4$. This can be understood by comparing the order parameter to its fluctuations at the correlation length-scale [19]:

$$\langle \delta\phi(\vec{r} = \xi(T))\delta\phi(\vec{r} = 0)\rangle - \phi_0^2 = G(\xi, 0) \ll \phi_0^2. \tag{1.10}$$

Using Eq. (1.8), one obtains how the correlation function scales with dimensionality, and from Eq. (1.3) and Eq. (1.9) we already know how the order parameter and correlation length scale with temperature:

$$G(\xi) \propto \xi(T)^{2-d} \propto |t|^{\frac{d-2}{2}} \ll |t| \propto \phi_0^2. \tag{1.11}$$

Hence, one can now easily see that for $d > 4$, in the $t \to 0$ limit the order parameter term dominates over the associated fluctuations. Conversely, for $d < 4$, fluctuations will prevail for $t \to 0$ and the mean-field approximation becomes thus inadequate for quantitatively predicting the corresponding critical behavior. In this sense, one often refers to $d = 4$ as the "upper critical dimension".

1.2.1 Critical Exponents and Universality

In the previous section, we discussed how critical points in the phase diagrams are linked to the divergence of the correlation length. This divergence leads to the independence of order parameter fluctuations with respect to any characteristic length scale at criticality. In simpler terms, fluctuations occur across all length scales, leading to a system characterized by scale invariance. This scale invariance directly results in power-law behavior of physical observables, as a power-law functional from lacks a characteristic scale. In fact, as long as the system is not precisely at its critical point, correlations still do decay exponentially, according to experiments and computations on mathematical models [20]. The introduced Landau-Ginzburg theory, then, features one of the simplest and most transparent description of the behavior of the diverging correlations length and of the related susceptibility when approaching the critical point, as well as, more in general, a second-order phase transition. Though less relevant here, this also applies to the temperature or field dependence of the order parameter, the specific heat, and other related quantities. All these kinds of behaviors are quantitatively described by the "critical exponents" such as those introduced above after Eq. (1.4) and Eq. (1.9) [7].

In Table 1.1, some of the most significant critical exponents describing the essential physics in the proximity of a second-order phase transition are listed along with the definitions of the associated observables. The values derived from Ginzburg-Landau theory in the mean-field approximation are shown in the row for MF values. Additionally, the table includes exponents for other *universality classes*. We briefly recall here that the crucial concept of "universality" implies that, as a consequence of the diverging correlation length at the 2nd order transition, the corresponding critical behavior is determined only by the dimensionality of the system, the symmetry of the order parameter, as well as the range of the microscopic interaction (here and in the following always assumed to be short range. Consequently, microscopically different phase transitions within the same universality class will exhibit identical critical exponents [7, 9, 18].

Observable	Exponent	Definition	MF value	3D Ising	3D Heisenberg
Specific heat	α	$C \propto \lvert t\rvert^{-\alpha}$	0	0.1	-0.08
Order parameter	β	$\phi \propto (-t)^{\beta}$	0.5	0.33	0.37
Susceptibility	γ	$\chi \propto \lvert t\rvert^{-\gamma}$	1	1.24	1.39
Correlation length	ν	$\xi \propto \lvert t\rvert^{-\nu}$	0.5	0.63	0.71
Correlation function	η	$G(r) \propto \lvert r\rvert^{-d+2-\eta}$	0	0.03	0.07

Table 1.1: Summary of critical exponents of most common 3D universality classes with their definitions (readapted from [7]). The mean-field (MF) values correspond to the exponents from Ginzburg-Landau theory.

Last, but not least, in order to complete the standard theoretical context, it is important to mention the Hertz-Millis-Moriya (HMM) theory [21–25], which is often considered as the conventional framework for describing quantum phase transitions in fermionic systems. In a nutshell, this approach extends the Landau-Ginzburg-Wilson (LGW) theory [26] by incorporating tem-

poral fluctuations relevant to the quantum regime. In particular, we recall that Hertz has first studied how temporal fluctuations can influence static and dynamical properties at zero and finite temperatures, and that, subsequently, Millis has investigated their influence on quantum phase transitions, predicting specific dynamical critical exponent values (z) for magnetic metallic systems [27, 28]. In the specific case of interest, i.e., for quantum phase transitions to 3D metallic spin-density wave ordering, the HMM theory yields the following values of for quantum critical exponents describing, respectively, the temperature dependence of the magnetic susceptibility and its associated correlation length: $\gamma = 1.5$ and $\nu = 0.75$ [27, 28]. However, the HMM theory faces relevant limitations, especially for strongly correlated metallic systems, where perturbative approaches may fail and/or where the low-energy excitations might behave differently than in conventional Fermi liquid systems. For instance, in such cases, the breakdown of the large Fermi surface [29, 30] or specific Fermi surface geometrical features [27], such as Kohn points, can lead to qualitative deviations from the HMM predictions and significantly different quantum critical behaviors [28].

Chapter 2

Theoretical Framework

"Great artists are people who find the way to be themselves in their art"

—*Margot Fonteyn*

In this chapter, we introduce the general formalism needed for our work, by defining the one- and two-particle quantities that build the foundation of our calculations. We then discuss Kohn anomalies on the Fermi surface within three-dimensional lattices. Thereafter, we provide a brief overview of the Hubbard Hamiltonian, which is the model specifically considered in our study, and of the Anderson impurity model, used to map the lattice model onto an auxiliary impurity model in the context of DMFT.

2.1 Important Quantities

In solid state physics we deal with an extensively high number of particles of the order 10^{23} per cm^3. Therefore, it is impossible to treat such systems exactly. However, most of the time a fully many-body description is not needed and many information are encoded in one- or two- particle quantities as well as in their embedding in an effective (in the easiest case: mean-field) medium describing their interaction with the rest of the system.

In this section we will briefly introduce the most important quantities for the calculations presented in our thesis, while for a more detailed discussion we refer the reader to various textbooks [31–34].

2.1.1 One-Particle Quantities

In the Green's function formalism, the simplest case corresponds to the definition of a propagator in momentum space describing the dynamics of an added/removed particle in the many-electron system

$$G_{i\sigma,j\sigma'}(\tau) = -\langle \mathcal{T} \hat{c}_{i,\sigma}(\tau) \hat{c}^{\dagger}_{j,\sigma'}(0) \rangle, \tag{2.1}$$

where τ is the Wick-rotated imaginary time, $\mathcal{T}$ the (imaginary) time ordering operator, $\hat{c}^{\dagger}_{j,\sigma'}$ and $\hat{c}_{i,\sigma}$, respectively the creation and annihilation operators and at site j with spin $\sigma' = \uparrow, \downarrow$ and at site i and spin $\sigma = \uparrow, \downarrow$, while $\langle ... \rangle = \frac{1}{Z}\mathrm{Tr}\{e^{-\beta H}\}$.

For a non-interacting system and in the absence of external fields, the Hamiltonian is given by $H = H_0 = \sum_{\mathbf{k},\sigma} \epsilon_k \hat{c}^{\dagger}_{\mathbf{k}\sigma}\hat{c}_{\mathbf{k}\sigma}$, where $\epsilon_{\mathbf{k}}$ is the energy momentum dispersion of the lattice. The one-particle Green's function, which is diagonal in spin space $G0, \sigma\sigma' = G_0\delta_{\sigma\sigma'}$ can be easily calculated explicitly:

$$G_0(\mathbf{k}, i\nu_n) = \frac{1}{i\nu_n - \epsilon_{\mathbf{k}} + \mu}, \tag{2.2}$$

where μ is the chemical potential and $i\nu_n = i\frac{(2n+1)\pi}{\beta}$ (with $\beta = 1/T$ and $n \in \mathcal{Z}$) are the fermionic Matsubara frequencies.

For an interacting system, however, where $H = H_0 + V$, with $V \neq 0$, the Green's function cannot, in general, be calculated explicitly. In this case, it is possible to systematically describe corrections to the non-interacting Green's function G_0 by introducing the electronic self-energy $\Sigma(\mathbf{k}, i\nu_n)$. This quantity corresponds, diagrammatically, to the collection of all topologically distinct 1-particle irreducible diagrams [35] and encodes crucial information about the renormalization of the low-energy fermionic excitation of the system. From a formal point of view, the self-energy builds the main core of the well-known Dyson equation:

$$G = (G_0^{-1} - \Sigma)^{-1} = \frac{1}{i\nu_n - \epsilon_{\mathbf{k}} + \mu - \Sigma}. \tag{2.3}$$

As we will see in the next chapter, Eq. (2.3) plays a central role in the self-consistency cycle of the dynamical mean-field theory (DMFT).

2.1.2 Two-Particle Quantities

On the two-particle level, we can in general define the corresponding following the conventions of Eq. (2.1)

$$G^{(2)}_{ijkl}(\tau_1, \tau_2, \tau_3) = \langle \mathcal{T}\, \hat{c}^{\dagger}_i(\tau_3)\hat{c}_j(\tau_2)\hat{c}^{\dagger}_k(\tau_1)\hat{c}_l(0)\rangle, \tag{2.4}$$

where i, j, k, l would be, in the most general case, combined spatial-spin-orbital indices.

If we restrict the definitions to the case of our specific interest, i.e., to the on-site (local) sin-

gle orbital two-particle Green's function the compound index reduces to just a spin index. In particular, the corresponding generalized susceptibility reads [36]

$$\chi_{\sigma_1\sigma_2\sigma_3\sigma_4}(\tau_1,\tau_2,\tau_3) = G^{(2)}_{\sigma_1\sigma_2\sigma_3\sigma_4}(\tau_1,\tau_2,\tau_3) - G_{\sigma_1\sigma_2}(\tau_1,\tau_2)G_{\sigma_3\sigma_4}(\tau_3,0). \tag{2.5}$$

The generalized susceptibility is directly connected to physical quantities, e.g. response functions that can be measured in experiments, and is therefore more commonly used than $G^{(2)}$. Using the Matsubara formalism by Fourier transforming Eq. (2.5) (s. [36–39] for details), as a result of the time-translational invariance and the SU(2)-symmetry of the problem, we get transformed quantities $\chi^{\nu\nu'\omega}_{\mathrm{ph/pp},\sigma\sigma'}$ which depend on two fermionic Matsubara frequencies ν, ν' and one bosonic/transfer frequency ω ($i\omega_n = i\frac{2n\pi}{\beta}$ with $n \in \mathcal{Z}$), as well as only two spins $\sigma, \sigma' = \uparrow, \downarrow$.

In general, a two-particle process described by the generalized susceptibility can be associated with a scattering of two particles (pp) or a particle and a hole (ph). Between the two so called channels, however, one can easily switch via a frequency/momentum shift [38–40]. Furthermore, due to the $SU(2)-$symmetry of the problem, we can spin-diagonalize [38][41] the generalized susceptibility, which corresponds to define the charge/density and spin/magnetic channel of the generalized susceptibility in the following way:

$$\chi^{\nu\nu'\omega}_{\mathrm{d}} = \chi^{\nu\nu'\omega}_{\mathrm{ph},\uparrow\uparrow} + \chi^{\nu\nu'\omega}_{\mathrm{ph},\uparrow\downarrow} \tag{2.6}$$

$$\chi^{\nu\nu'\omega}_{\mathrm{m}} = \chi^{\nu\nu'\omega}_{\mathrm{ph},\uparrow\uparrow} - \chi^{\nu\nu'\omega}_{\mathrm{ph},\uparrow\downarrow}. \tag{2.7}$$

Summing over the Matsubara frequencies in the channels above yields the corresponding charge/-density or spin physical response of the system to an external field [39].

From the diagrammatic point of view, the susceptibility in Eq. (2.5) can be decomposed into connected and disconnected diagrams, whereas the latter ones can be expressed in terms of the full vertex function F, which entails all possible "vertex corrections". Specifically, F describes all fully connected two-particle processes where all external legs are interconnected [1]. The generalized susceptibility can then be explicitly written as

$$\chi^{\nu\nu'\omega}_{\sigma\sigma'} = -\beta G_\sigma(\nu)G_\sigma(\nu+\omega)\delta_{\nu\nu'}\delta_{\sigma\sigma'} - G_\sigma(\nu)G_\sigma(\nu+\omega)F^{\nu\nu'\omega}_{\sigma\sigma'}G_{\sigma'}(\nu')G_{\sigma'}(\nu'+\omega). \tag{2.8}$$

[1] Formally, we consider the 1-particle irreducible diagram subset among all 2-particle processes.

The first term describes an independent propagation of a particle and a hole, without interaction with each other and is often called "bubble" contribution

$$\chi_{0,\sigma\sigma'}^{\nu\nu'\omega} = -\beta G_\sigma(\nu) G_{\sigma'}(\nu+\omega)\delta_{\nu\nu'} = -\beta G(\nu) G(\nu+\omega)\delta_{\nu\nu'}\delta_{\sigma\sigma'} = \chi_0^{\nu\nu'\omega}, \tag{2.9}$$

where we have exploited, once again, the SU(2)-symmetry. Evidently, the susceptibility bubble contains only one-particle Greens's functions and is therefore much easier to compute than the generalized susceptibility. At the same time, due to the lack of any two-particle scattering process, the bubble term is, in general, an insufficient approximation.

In my previous project work [42] we used the non-interacting susceptibility bubble to identify Fermi surface nesting by searching for the maximum of χ_0. As a consequence, our algorithm was able to show, whether special geometrical features, such as Kohn points, which we are going to discuss in details in the next section, are present in the chosen Fermi surface. "Kohn anomalies" are primarily encoded in the momentum-dependent susceptibility bubble and their physics might be remain somewhat unaffected by the local (i.e., momentum-independent) self-energy and irreducible vertex corrections of DMFT. Therefore, to counter increasing the complexity of our methods to study the quantum criticality of strongly correlated electron systems, we will perform semi-analytical detailed studies of the momentum-dependence of the bubble term, especially when trying to classify the geometrical properties of the underlying Fermi surface. In the next section, we want to present the main finding of [42].

2.2 Kohn Anomalies of the Fermi Surface

Among several important aspects controlling the phenomenon of quantum criticality, we focus here on the special influence that specific geometrical properties of the Fermi surface can exert. Parts from the following section are taken and slightly readopted from my project work [42]. These sections are indicated by a black bar along the outer margin of the page.

> In particular, important information can be already encoded in the one-particle properties, whose special features may significantly influence the behavior of strongly correlated electron systems, and, in particular, its tendency towards instabilities. For instance, while peaks in the density of states, like those resulting from van Hove singularities, can induce ferromagnetism, in a similar way, Fermi surface nesting tends to lead to the formation of spin density waves. Although perfect nesting is rather uncommon, spin density waves can nonetheless arise from the so-called "local" nesting near specific points on the Fermi surface.
>
> More specifically, back in 1959 W. Kohn explored the impact of this "local" nesting [43], demonstrating that the susceptibility of systems with a spherical Fermi surface depends *non-analytically* on momentum near wave-vectors of length $Q = 2k_F$. Points on opposite sides of

the Fermi surface, which are connected by these vectors Q and additionally possess opposite Fermi velocities are known as "Kohn points". While the non-analytical peculiarity is generally subtle, it can give rise to significant phenomena such as anomalies in phonon frequencies and the Kohn-Luttinger mechanism of superconductivity [44].

In essence there are two simple conditions, which have to be fulfilled for the appearance of Kohn anomalies on the Fermi surface:

Kohnpoints are defined as a set of two distinct points on the Fermi surface with the following properties:

1. They are connected via the SDW ordering vector (nesting)
2. They have opposite (antiparallel) Fermi velocities v_F

Recently we developed an algorithm [42], which allowed us to identify Kohn points of the Fermi surface in three dimensions for various lattice geometries, where Kohn points can appear isolated or forming a line of points on the Fermi surface. Here we want to present the main results of [42], which set the base for our investigation of the influence of these Fermi surface properties on the magnetic quantum criticality in 3D lattices.

2.2.1 Simple Cubic Lattice

In the simple cubic lattice, as illustrated in Fig. 2.1, we find lines of Kohn points in a range of the chemical potential $\mu = [-2t, 2t]$. More specifically there are four pairs of lines of Kohn points $(\pm K_x, \mp K_x - \pi, -Q_z/2)$ and $(\pi \pm K_x, \mp K_x, Q_z/2)$ which are connected by the ground-state spin density wave-vectors $Q_0 = (\pi, \pi, Q_z)$ (and symmetrically equivalent wave-vectors). Additionally $K_x \pm K_y = \pm\pi$ and $K_z = -Q_z/2 = -\arccos(-\mu/(2t))$.

Due to the symmetry of the Fermi surface ($\mu \to -\mu$ being equivalent to $k \to 2\pi - k$), we can restrict our presentation to the cases with positive values of μ. At the very special condition of half filling ($\mu = 0$) which corresponds to perfect particle hole symmetry the whole Fermi surface displays perfect nesting: Each point of the Fermi surface is connected by $Q = (\pi, \pi, \pi)$ to its "partner", while possessing opposite Fermi velocities. This makes the *whole* Fermi surface fulfilling antiparallelitions for Kohn points. With increasing the chemical potential μ, a couple of lines of Kohn points are identified, connected by a vector $Q = (\pi, \pi, Q_z < \pi)$ $Q_z = 2\arccos(-\mu/2t))$. This deviation from the antiferromagnetic order $Q = (\pi, \pi, \pi)$ is called incommensurability and leads to the formation of a spin-density wave (SDW). Due to the cubic symmetry, this can obviously appear in each of the three momentum directions $Q = (\pi, Q_y, \pi)$, $Q = (Q_x, \pi, \pi)$ or $Q = (\pi, \pi, Q_z)$. In Fig. 2.1 we show the (one) line of Kohn points K, where its "partners" $K + Q$ remain in the first Brillouin zone. Varying the values of μ one can see the Q-vector changes from (π, π, π) at $\mu = 0$ to $(\pi, \pi, 0)$ at $\mu = 2$ (with t=1) corresponding to the limits of $Q_z = 2\arccos(-\mu/2t)$. At larger fillings ($|\mu| > 2$) no points on the Fermi surface fulfill the criterion of the Kohn points anymore.

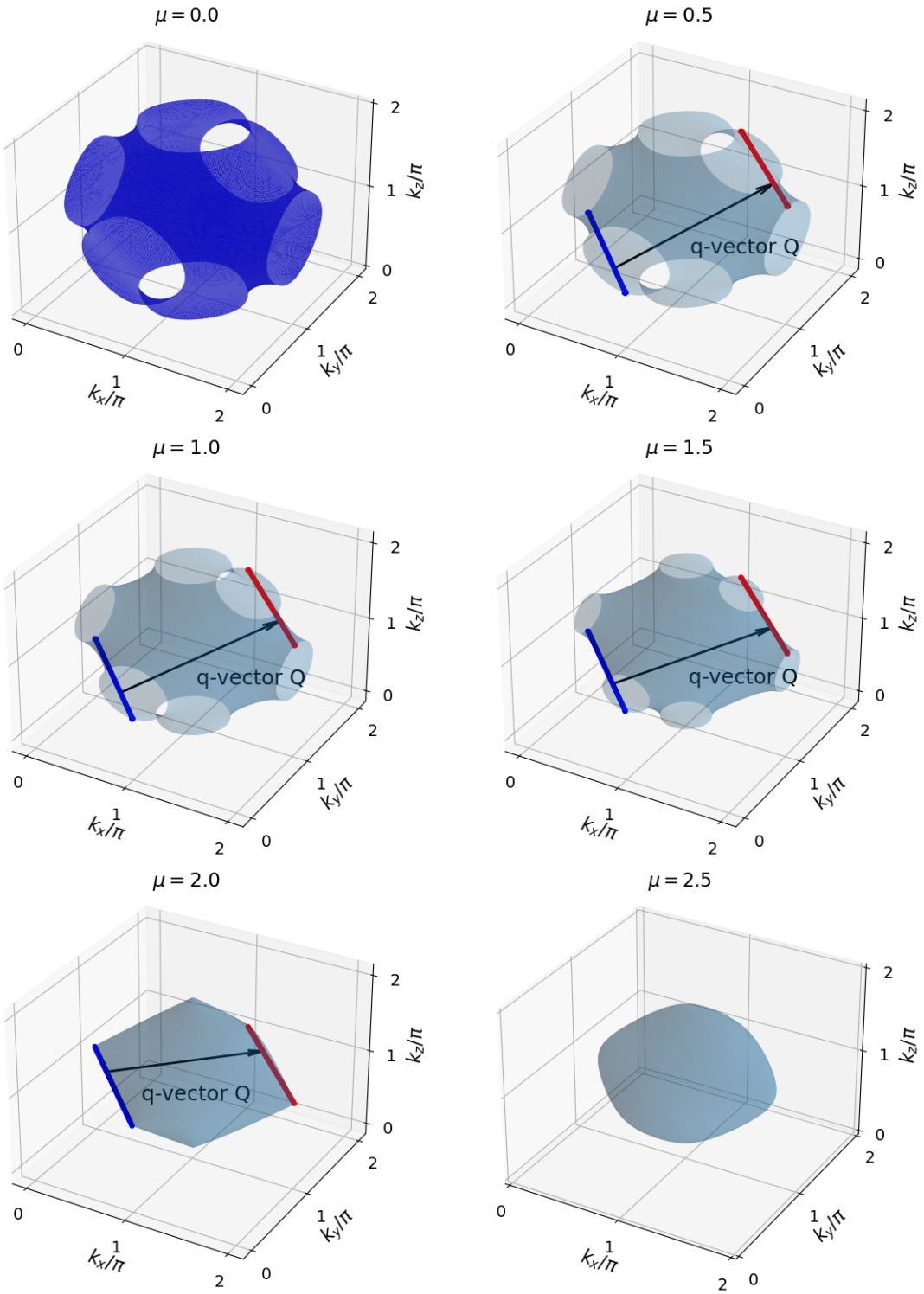

Figure 2.1: (Plot and caption taken from [42]) Fermi surfaces with Kohn points K in blue and K+Q in red for the simple cubic lattice. At $\mu = 0$ the whole Fermi surface meets the requirement of being a Kohn point, due to perfect nesting. With increasing of the chemical potential μ lines of Kohn points K emerge connected by the vector $Q = (\pi, \pi, Q_z)$ to the Kohn points K+Q. The value of Q_z varies from π at $\mu = 0$ to 0 at $\mu = 2$. At $|\mu|$-values larger than 2 no Kohn points exist anymore.

2.2.2 Frustrated Cubic Lattice

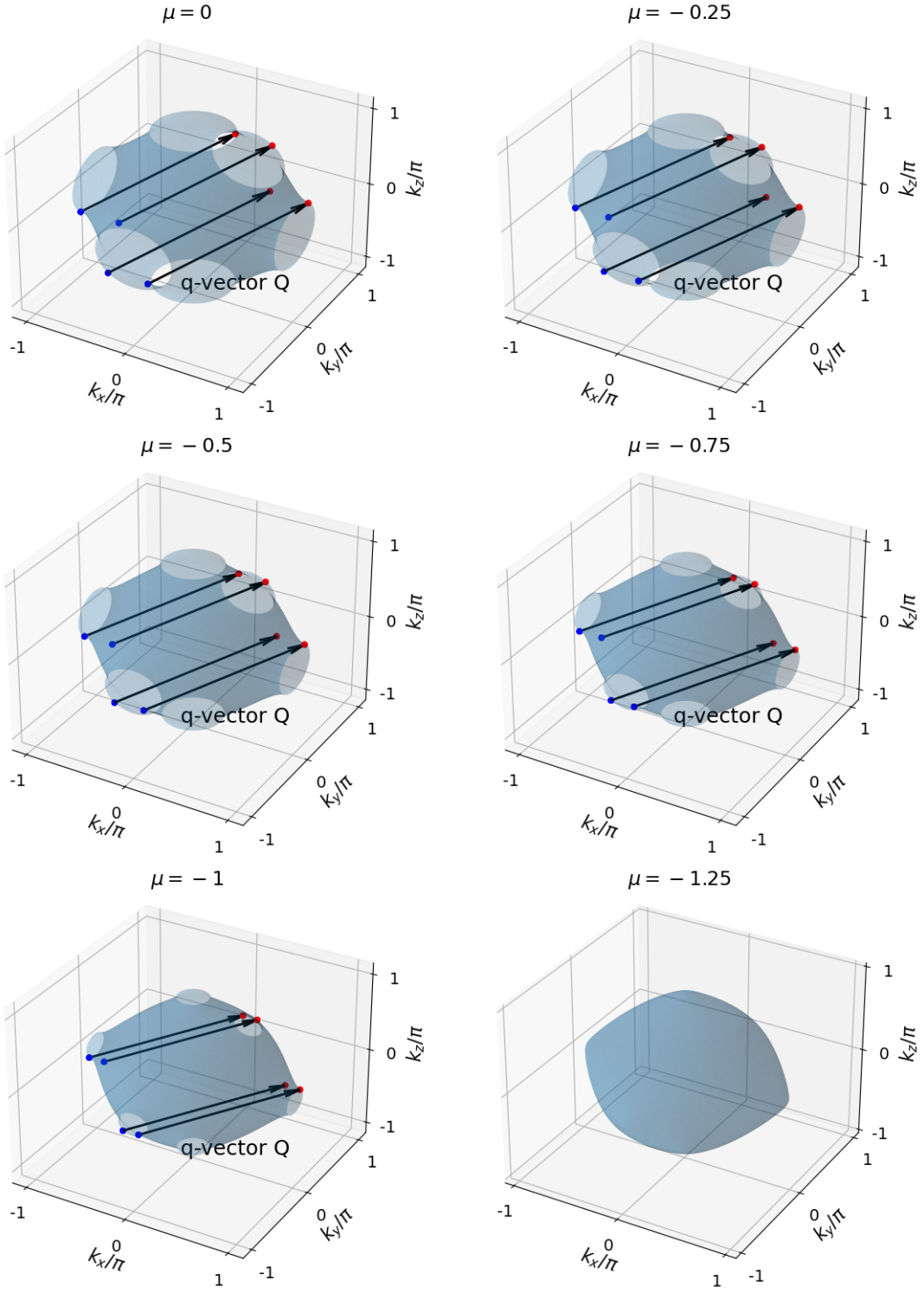

Figure 2.2: (Plot and caption taken from [42]) Fermi surfaces with Kohn points K in blue and K+Q in red for the frustrated cubic lattice with $t' = 0.2t$. Isolated Kohn points K emerge connected by the vector $Q = (\pi, \pi, Q_z)$ to the Kohn points K+Q. For $\mu = -1.25$ no Kohn points exist anymore.

With the simple cube as a starting point one can add the next nearest neighbor hopping t' contribution to the dispersion relation. In particular, we choose $t' = 0.2$ and noticed, that at the chemical potential of $\mu = t'$ the Q-vector reads $\vec{Q} = (\pi, \pi, q_z = \pi)$. When lowering μ, two components remain fixed, while the third one decreases: $\vec{Q} = (\pi, \pi, q_z < \pi)$. Therefore in the range of the chemical potential $\mu \sim \left[-1.2t, 0.2t\right]$ the Q-vector appears on a high symmetry path, where two momentum components are π (comparable situation with the simple cubic case). Around $\mu = 1.2$ the changing component reaches 0, setting the limit for the appearance of Kohn points.

At difference from the simple cube, where Kohn points appeared along couple of lines, due to geometrical frustration, isolated Kohn structures emerge. Specifically, for $\vec{Q} = (\pi, \pi, Q_z)$, 12 isolated Kohn points appear (always 3 points in a closer area together). Four of those Kohn points K have partners K+Q in the first Brillouin zone, as displayed in Fig. 2.2. We should note, here, that more analytical descriptions of Kohn points in the frustrated cube are not easy to derive, due to the more complex dispersion relation compared to the simple cube.

The most significant effect of Kohn anomalies on magnetic properties occurs when the wave-vector Q, linking Kohn points, corresponds to a global maximum of susceptibility. In this case, Q coincides with a wave-vector of a spin- or charge-density wave. Determining whether the susceptibility features a global maximum typically relies on the entire electronic structure, often requiring numerical ab-initio calculations or experimental momentum resolved spectroscopic investigation. However, the existence of a local maximum in susceptibility can be inferred from the local geometry of the Fermi surface near Kohn points [45].

2.3 Models

In the following subsections, we will introduce the Hubbard model, which we use to describe electronic correlations in three-dimensional lattice systems of bulk metals through DMFT and RPA calculations. Thereafter, we will also define the Anderson impurity model (AIM), as it represents an essential building block for the DMFT self-consistent algorithm, as we will recall in the next chapter. Parts from the following section are taken and slightly readopted from my Bachelor thesis [46]. These sections are indicated by a black bar along the outer margin of the page.

2.3.1 Hubbard Model

In solid state theory of correlated electrons Hamiltonians, containing only relevant fundamental interactions can be constructed [47]. A famous example is provided by the Hubbard model, which captures among many fascinating phenomena, the transition between conducting and Mott-insulating phases [48, 49]. In its simplest realization, this model considers the electron

hopping between neighboring lattice sites (kinetic energy term) and the Coulomb-interaction between electrons with opposite spin, occupying the same lattice site (potential energy term). The Hamiltonian of the Hubbard model in second quantization and grand canonical ensemble is given by:

$$\hat{H}_{\mathrm{HM}} \equiv \hat{H} = -t \sum_{\langle ij \rangle, \sigma} [\hat{c}^{\dagger}_{i\sigma} \hat{c}_{i\sigma} + h.c.] + U \sum_{i} \hat{n}_{i\uparrow} \hat{n}_{i\downarrow} - \mu \sum_{i,\sigma} \hat{n}_{i\sigma} \ , \tag{2.10}$$

where the first term describes the electron-hopping and the second term the Coulomb-interaction. t is the hopping integral, μ the chemical potential, U corresponds to the strength of the screened on-site Coulomb-repulsion, $\hat{c}_{i\sigma}$ is the annihilation and $\hat{c}^{\dagger}_{i\sigma}$ the creation operator for an electron with spin σ on the site i, while $\hat{n}_{i\sigma} = \hat{c}^{\dagger}_{i\sigma} \hat{c}_{i\sigma}$ is the spin-density operator.

Generally, there are no exact solutions known for the Hubbard model in arbitrary dimensions. The difficulty arises from the fact, that the hopping term is diagonal in momentum space, while the interaction term is diagonal in real space. Obvious exceptions are the two special limiting cases, where $U = 0$ or $t = 0$. In the first case, the electrons can move freely and can be described by Bloch-waves. In the other case ($t = 0$) the electrons are fully localized and the system can be decomposed into infinitely many copies of the atomic limit. In presence of finite U and T, the Hubbard model can be solved exactly only in one dimension via the Bethe Ansatz [50] and in infinite dimensions via the dynamical mean field theory (DMFT) [51].

2.3.2 Anderson Impurity Model

The Anderson impurity model (AIM) describes a single impurity-site coupled to a non-interacting bath of conduction electrons. Its corresponding Hamiltonian reads:

$$\hat{H}_{\mathrm{AIM}} = \sum_{l\sigma} \epsilon_l \hat{a}^{\dagger}_{l\sigma} \hat{a}_{l\sigma} + \sum_{l\sigma} V_l (\hat{c}^{\dagger}_{\sigma} \hat{a}_{l\sigma} + \hat{a}^{\dagger}_{l\sigma} \hat{c}_{\sigma}) + U \hat{n}_{\uparrow} \hat{n}_{\downarrow} - \mu (\hat{n}_{\uparrow} + \hat{n}_{\downarrow}) \tag{2.11}$$

$\hat{a}^{\dagger}_{l\sigma}$ and $\hat{a}_{l\sigma}$ create and annihilate an electron with spin σ with energy ϵ_l (at the bath-level), while $\hat{c}^{\dagger}_{\sigma}$ and $\hat{c}_{\sigma}$ create and annihilate an electron at the impurity site (with $\hat{n}_{\sigma} = \hat{c}^{\dagger}_{\sigma} \hat{c}_{\sigma}$). The hybridization between the bath and the impurity is characterized by V_l, U is the on-site repulsion between two electrons at the impurity and μ the chemical potential. The AIM is a useful model for the representation of the lattice system's purely local correlations in the context of DMFT calculation.

Chapter 3

Methods: Computing Magnetic Susceptibilities and Correlation Lengths

"If the gods make the wrong decision, what should I do?"

—*Samuel Badr*

In this chapter, we briefly introduce the methods and the algorithms used to compute the magnetic susceptibility and the magnetic correlation length. Starting with the non-interacting bubble, we incorporate correlations using the random phase approximation (RPA). Finally, we present the dynamical mean-field theory (DMFT), a powerful and widely used approach in the study of strongly correlated systems.

3.1 Bubble Computation and RPA

Previously we introduced the susceptibility bubble in Eq. (2.9). Now, we will consider the isothermal/static response $\chi_0(\mathbf{q})$ for the non-interacting case, obtained after performing the summation over the internal fermionic Matsubara frequencies in the bubble term of the generalized susceptibility, and setting the bosonic Matsubara frequency $\omega = 0$. As it is well known, this way one obtains the famous Lindhard function:

$$\chi_0(\mathbf{q}) = -\frac{1}{N_k} \sum_k \frac{f(\epsilon_{\mathbf{k}+\mathbf{q}}) - f(\epsilon_{\mathbf{k}})}{\epsilon_{\mathbf{k}+\mathbf{q}} - \epsilon_{\mathbf{k}}}. \tag{3.1}$$

Here $f(\epsilon_{\mathbf{k}})$ is the Fermi function, $\epsilon_{\mathbf{k}}$ the one-particle energy-momentum dispersion of the lattice, as it appears in the non-interacting Hamiltonian, and the normalization prefactor N_k the number of momenta of the selected grid.

One of the simplest methods to add interaction to the bubble susceptibility is the random phase approximation (RPA). Among others, RPA can describe collective excitations and electronic screening effects beyond Thomas-Fermi. It uses a perturbative approach at the level of the polarization function to derive a screened potential and, consequently, the screened susceptibility reading

$$\chi_{m,\mathrm{RPA}}(\mathbf{q},\omega) = \frac{\chi_0(\mathbf{q},\omega)}{1 - U\chi_0(\mathbf{q},\omega)}, \tag{3.2}$$

with an interaction potential U. In our calculations, we have already assumed that the bare electronic interaction is represented by the momentum-independent, on-site electrostatic Hubbard repulsion. Additionally, we will consider the isothermal/static response by setting $\omega = 0$, just as we did for the non-interacting bubble.

3.2 DMFT

The Hubbard model introduced in the previous section can not be solved analytically in dimensions $d > 1$ [52] and numerically "exact" only in certain parameter regimes [53]. Therefore, approximative approaches are necessary in order to solve the Hubbard model in two or more dimensions. One very famous among such approximative schemes is the dynamical mean-field theory (DMFT). DMFT neglects all non-local spatial fluctuations beyond static mean-field by introducing a self-consistently determined effective field around a selected single lattice site. Practically, this is realized by mapping a lattice model to an auxiliary impurity model (AIM). Differently from a static mean-field theory e.g. the RPA presented above, however, in DMFT no average over time is made, as the dynamical structure of the introduced effective field is fully retained.

Formally, this allows to compute frequency (but not momentum!) dependent irreducible one- and two-particle quantities, such as the on-site self-energy and the irreducible two particle vertex function. This shows how, in DMFT temporal correlations are not neglected in contrast to the RPA, providing a powerful, non-perturbative framework for studying strongly correlated electron systems.

In practice, DMFT is computed numerically via a self-consistency loop. The DMFT approach maps the lattice model to an auxiliary AIM (2.11), which consists of an interacting impurity coupled to a non-interacting bath. The hybridization with this bath acts as a dynamic mean-field that is iteratively updated until convergence is achieved. As we will shortly recall in the following subsections, the key quantities in this process are the lattice Green's function $G(i\nu_n, k)$ and the impurity Green's function $G(i\nu_n)$. By describing the self-consistency loop we will follow the implementation in [54] restricted to the specific SU(2)-symmetric, single-orbital case of our interest, as well as a further detailed discussion in [55]. Subsequently, we will highlight the

procedure followed in the post-processing of the DMFT data for the specific task of computing the magnetic correlation length.

The self-consistency loop involves several steps: In the first one the hybridization function Δ between the AIM bath and the local impurity is determined through the relation:

$$\Delta(i\nu_n) = i\nu_n + \mu - \left(\frac{1}{N_k} \sum_{\mathbf{k}} G_0(\mathbf{k}, i\nu_n) \right)^{-1}, \tag{3.3}$$

where $G_0(\mathbf{k}, i\nu_n)$ is the non-interacting lattice Green's function in momentum/Matsubara frequency space. In the next step, the non-interacting Green's function for the impurity site of the AIM is expressed as:

$$G_{0,\mathrm{AIM}}(i\nu_n) = [i\nu_n + \mu - \Delta(i\nu_n)]^{-1}. \tag{3.4}$$

Then, the interacting impurity model is solved using a specific semi-analytical and/or numerical algorithm [51] to obtain the interacting impurity Green's function $G(\nu_n)$. The corresponding impurity self-energy can be extracted by inverting the Dyson equation of the AIM:

$$\Sigma(i\nu_n) = [G_{0,\mathrm{AIM}}(i\nu_n)]^{-1} - [G(i\nu_n)]^{-1}. \tag{3.5}$$

Assuming that the self-consistency relation of DMFT already holds, the interacting lattice Green's function would read:

$$G(\mathbf{k}, i\nu_n) = \left[(G_0(i\nu_n, k))^{-1} - \Sigma(i\nu_n) \right]^{-1}. \tag{3.6}$$

In order to check, whether the self-consistency relation of DMFT was actually fulfilled, in the last step of the cycle the local (i.e., on-site) interacting Green's function of the lattice $G_{\mathrm{loc}}(i\nu_n)$ is computed by averaging over all k-points:

$$G_{\mathrm{loc}}(i\nu_n) = \frac{1}{N_k} \sum_{\mathbf{k}} G(\mathbf{k}, i\nu_n). \tag{3.7}$$

This function is then compared to the interacting impurity Green's function $G(i\nu_n)$. If they coincide within a specified error range, the DMFT calculation is considered converged. Otherwise, the process must be iterated by updating the non-interacting impurity Green's function. The input for the new cycle would be then:

$$G_{0,\mathrm{AIM}}(i\nu_n) = \Big[(G_{\mathrm{loc}}(i\nu_n))^{-1} + \Sigma(i\nu_n)\Big]^{-1}. \tag{3.8}$$

Hence, in a nutshell, the DMFT self-consistency loop links these models using the hybridization function Δ and the impurity/lattice on-site (local) self-energy Σ_{loc}, iterating until the impurity and the on-site lattice Green's functions converge. This iterative procedure effectively captures a major part of the electronic correlation (i.e., its purely local part) originated by the interplay between the on-site Hubbard interaction and electronic hopping processes occurring in the lattice structure, without resorting to any perturbative approximation/expansion. This renders the DMFT a well suited tool for studying correlated electron systems in their intermediate-to-strong coupling regime.

Finally, we want to briefly mention some of the most used algorithmic procedures to solve the Anderson Impurity Model (AIM) numerically. Once again, a more detailed discussion is presented in [54]. Two commonly used methods are continuous-time Quantum Monte Carlo (CT-QMC) [56] and exact diagonalization (ED) [57–60]. These approaches complement each other. In ED, the infinitely large Hilbert space of the bath is approximated by representing it with a finite number of states, which are then solved exactly through direct diagonalization and/or Lanczos [51].

On the other hand, nowadays, the most advanced DMFT schemes often exploit CT-QMC algorithms. These tackle the full complexity of the Hilbert space of the auxiliary AIM using the path integral formalism. In spite of the unavoidable statistical errors, the CT-QMC solver is often the method of choice to handle more complex impurity models, such as multi-band calculations, cluster extensions of DMFT [61] or particularly challenging parameter regimes. For that reason, in this thesis, differently from previous studies [45] performed with ED, we have used the w2dynamics [62, 63] implementation of the CT-QMC as impurity solver for our DMFT calculations. Without delving into the details of the w2dynamics implementation, we just recall here that this CT-QMC package is based on the so-called "hybridisation expansion" (or also: "strong-coupling expansion") scheme of CT-HYB [56].

3.3 Computing Susceptibilities and Correlation Lengths

Having introduced all the necessary definitions in the previous section, we will now shortly illustrate how we computed the key quantities for this work. We begin by analyzing the susceptibility bubble, which is then incorporated into the RPA framework. Finally, we will provide more details of our DMFT workflow.

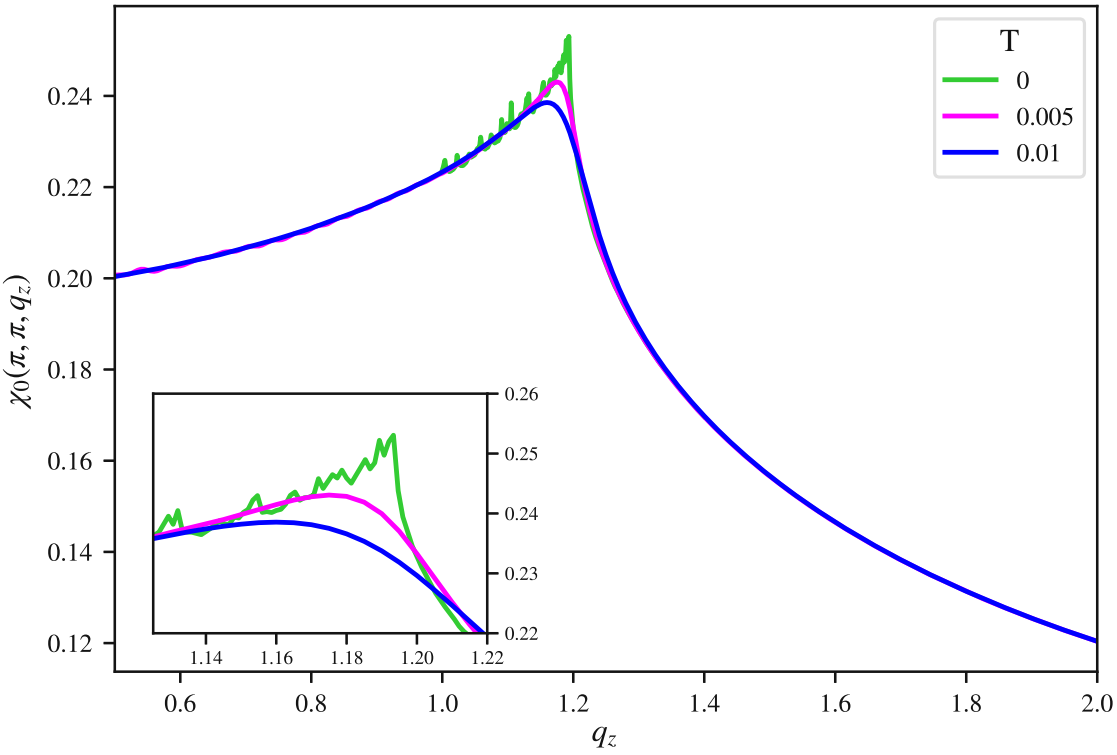

Figure 3.1: Susceptibility bubble $\chi_0(\mathbf{q})$ of the simple cubic lattice for $\mu \approx 1.65$ as a function of $\mathbf{q} = (\pi, \pi, q_z)$ for $T = 0$ and two finite temperatures. The width and position of the peak changes with temperature [45].

3.3.1 Characteristics of the Susceptibility Bubble

The susceptibility bubble can be computed using the Lindhard formula Eq. (3.1). To identify Kohn points we used the $T \to 0$ limit, where we could identify the nesting vector Q at the susceptibility maximum. In section 2.2 we illustrated how Kohn lines can appear in the simple cubic lattice (cf. also [45, 64]) and isolated Kohn points, among others possibilities [64], in the frustrated cubic lattice [42]. Therefore, we have focused on this two specific lattices for our calculations.

When computing the non-interacting susceptibility $\chi_0(\mathbf{q})$ for the simple cubic lattice, the maximum appears along a high symmetry path $\overline{MR}$ (for $|\mu| < 2t$ [45]), corresponding to $\mathbf{q} = (\pi, \pi, q_z)$. Hence, we can restrict the computation to this path. At $T = 0$ we get

$$\chi_0(q_z) \equiv \chi_0(\pi, \pi, q_z) = -\frac{1}{N_k} \sum_k \frac{\Theta(\epsilon_{\mathbf{k}+q_z}) - \Theta(\epsilon_{\mathbf{k}})}{\epsilon_{\mathbf{k}+q_z} - \epsilon_{\mathbf{k}}}, \tag{3.9}$$

with theta-functions replacing the Fermi functions in the $T \to 0$ limit. Fig. 3.1 shows the corresponding results for $\chi_0(q_z)$ for $\mu \approx 1.65$ in the range of $q_z = [0.5, 2]$ for $T = 0$, as well as, $\beta = \frac{1}{T} = 100$ and $\beta = 200$. We only display positive values of q_z, the susceptibility being

symmetric around $q_z = 0$ for $q_z = [-\pi, 0]$ due to the cubic geometry of the lattice. Analytical expressions for the position of the peak and the behaviour of $\chi_0(q_z)$ are explicitly discussed in the supplemental material of [45]. One remarkable feature of the susceptibility bubble at zero temperature is the cusp-like nature of the peak, which as a direct consequence of the non-analytic momentum dependencies originated from the Kohn anomalies on the Fermi surfaces [45, 64]. On the other hand, at finite temperatures, the non-analytic behavior is no longer present: As it can clearly be seen in Fig. 3.1, the corresponding peak becomes gradually smoother and broader as the temperature increases.

3.3.2 Numerical Extraction of the Correlation Length

In the next step we can apply the RPA Eq. (3.2), which is a simple static mean-field approach. Depending on the chemical potential μ (corresponding to a density n) and the interaction strength U the susceptibility is enhanced up to the limit where $U\chi_0(\mathbf{q}) = 1$, which corresponds to a divergence of $\chi_{m,\mathrm{RPA}}$, characterizing a second-order phase transition. A similar trend, though with significant quantitative differences, happens for the enhancements and (in some case) the divergence of the magnetic susceptibility in DMFT.

While the numerical DMFT and RPA results will be presented in the next chapter, here, we will illustrate the procedure we used to extract correlation length ξ from the momentum dependence of the magnetic susceptibility. Let us recall the correlation function from the Ginzburg-Landau theory

$$G(r) \propto \frac{e^{-r/\xi(T)}}{r^{(d-1)/2}} \xi^{(3-d)/2}. \tag{3.10}$$

Now, we will consider the three dimensional case and introduce the Ornstein-Zernike function, describing the susceptibility comparable to the correlation function above

$$G(\vec{r}) \sim \chi(\vec{r}) \sim \int d^3k \frac{e^{i\vec{k}\vec{r}}}{|\vec{k}|^2 + \xi^{-2}} \sim \frac{e^{-\vec{r}/\xi}}{\vec{r}}. \tag{3.11}$$

Hence, along a q_z-cut in momentum space around $\mathbf{q}_{max} = (\pi, \pi, \bar{q}_z = \pi - \delta)$, we will have

$$\chi_m(q_z, T) = \frac{\mathcal{A}(T)}{(q_z - \bar{q}_z)^2 + \xi^{-2} + \mathcal{C}(q_z - \bar{q}_z)^3}, \tag{3.12}$$

with a temperature dependent parameter $\mathcal{A}(T) \geq 0$, which essentially parameterizes the overall weight of the OZ-shape maximum, and $\bar{q}_z$ indicating the q_z-momenta for which the maximum of the susceptibility is found. It is important to underline, here, that in Eq. (3.12) we have added a higher order term in $(q_z - \bar{q}_z)$ to account for the asymmetry of our susceptibilities around its

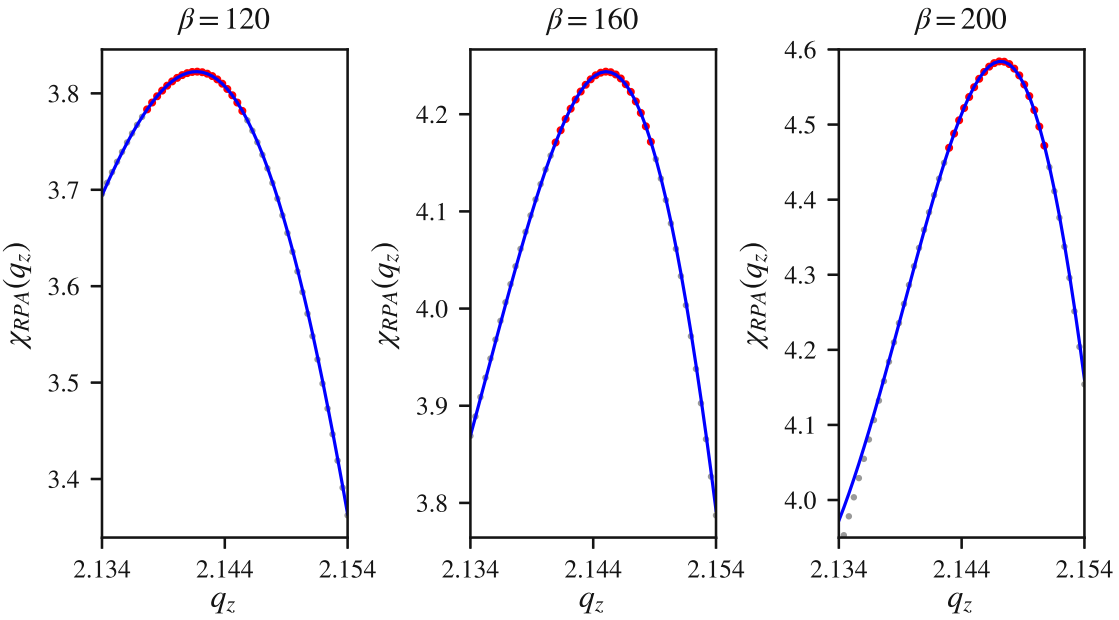

Figure 3.2: RPA susceptibility of the Hubbard model with $U = 3$ on the simple cubic lattice at a density of $n = 0.73$. The blue line indicates an Ornstein-Zernike fit of the red highlighted data points around the susceptibility peak. The value of the maximum, the position and the width of the peak change with the three temperatures displayed.

maximum (see Fig. 3.1). It is also important to recall here, as a warning, that the expression Eq. (3.12) is only valid around the maximum of $\chi_m(q_z, T)$, and that, depending on the situations, the q_z-interval of its applicability can become quite narrow.

In Fig. 3.2 fits of the RPA susceptibility data with the Ornstein-Zernike formula are displayed for the simple cubic lattice at a doping of $n = 0.73$ with $U = 3$ and for three different temperatures. With this procedure we can extract the correlation length $\xi(T)$ along a chosen path along the Brillouin zone.

Comparing the maximum values and width of the susceptibility-peaks computed in Fig. 3.2 indicates a well defined trend in the temperature scaling which we will discuss in more detail in the next chapter. While the susceptibilities of the simple cubic lattice are shown above, for the frustrated cubic lattice the procedure of extracting the correlation length is exactly the same.

3.3.3 Numerical Limitations in 3D

Performing plain numerical bubble and RPA calculations in three dimensional lattices can lead to a (somewhat unexpectedly) high numerical effort, due to the sum over all Brillouin zone k-points in Eq. (3.1). In the presence of a strong susceptibility enhancement in RPA around $U\chi_0(\mathbf{q}) \sim 1$ (i.e. in the proximity of the phase transition) we need the sharp peak to be properly resolved. As a consequence, our procedure of extracting the correlation length with a fit around the maximum of the susceptibility can become highly sensitive w.r.t. otherwise small numerical

errors. In particular, if the amount of k-points of the internal k-summations is not sufficiently high, significant deviations from converged results can appear (and fitting routines might then break down). In our RPA calculations, for the lowest temperatures we used at least 1000^3 k-points, mostly even 1500^3. Interestingly, the determination of the maximal value of $\chi_{m,\mathrm{RPA}}(\mathbf{q})$ is less sensitive than the correlation length: It converges already for a much lower amount of k-points (e.g., $200^3 - 400^3$) in the temperature range considered.

3.4 Workflow of DMFT

In the previous section we introduced a way of computing the susceptibility and correlation length in a static mean-field. Going beyond in the following we will use DMFT to compute a q-dependent $\chi_{\mathrm{ch,sp}}$, since it is build from the momentum dependent interacting lattice Green's functions and the vertex function. Once again we will follow the discussion in [54] about our work flow of the DMFT computations.

Restricting the calculation to the static case the single-band Hubbard model in the particle hole sector reads:

$$\chi_m(\mathbf{q},\omega{=}0) = \frac{1}{N_k\beta^2}\sum_{\mathbf{k}\mathbf{k}'}\sum_{\nu\nu'} -\beta G^{\nu}_{\mathbf{k}} G^{\nu'}_{\mathbf{k}'+\mathbf{q}}\delta_{\nu\nu'} + G^{\nu}_{\mathbf{k}} G^{\nu}_{\mathbf{k}'+\mathbf{q}} F_m^{\nu\nu'}(\mathbf{q}) G^{\nu'}_{\mathbf{k}} G^{\nu'}_{\mathbf{k}'+\mathbf{q}}, \tag{3.13}$$

with N_k being the total k-point number of our grid in the Brillouin zone (note that, here, we have adopted a short-hand notation for the one-particle DMFT Green's function (i.e. $G^{\nu}_{\mathbf{k}} = G(\mathbf{k}, \mathbf{i}\nu)$) and $F_m^{\nu\nu'}(\mathbf{q})$ the full scattering DMFT vertex for the considered lattice in the magnetic channel.

Evidently, a divergence in the static/isothermal susceptibility $\chi_m(\mathbf{q})$ at $\mathbf{q} = (\pi, \pi, \pi)$ would correspond to the emergence of a commensurate (3D-checkerboard, G-type) antiferromagnetic order, while if the divergences appears for $\mathbf{q} = (\pi, \pi, q_z < \pi)$ the system will manifest an instability towards an *incommensurate* antiferromagnetic order ("i-AF"). The generalized static spin/magnetic susceptibility in DMFT reads: [38, 39, 51, 65]:

$$\chi^{\nu\nu'}_{\mathrm{m,DMFT}}(\mathbf{q}) = \left[[\chi_0^{\nu\nu'}(\mathbf{q})]^{-1} + \Gamma^{\nu\nu'}_{\mathrm{m}}\right]^{-1}, \tag{3.14}$$

where $\Gamma^{\nu\nu'}_{\mathrm{m}}$ is the (dynamical) two-particle irreducible vertex function of the auxiliary AIM. It is important to note, here, that, as a consequence of the purely local nature of $\Gamma^{\nu\nu'}_{\mathrm{m}}$ in the DMFT context [51, 66], explicit momentum-dependent features such as the Kohn anomalies on the Fermi surface are essentially encoded in the momentum-dependence of the "dressed" bubble term $\chi_0^{\nu\nu'}(\mathbf{q})$ (build up with the product of two interacting lattice Green's function of DMFT).

As for the actual implementation of the DMFT calculations, one should carefully consider the high sensibility of $\chi_m(\mathbf{q})$ w.r.t. small density changes as well as tiny numerical uncertainties. Evidently, such sensitivity poses a challenging task. In order to obtain numerical results of sufficient accuracy for the quantum critical properties of the Hubbard model on a simple cubic lattice by means of our DMFT simulations, exploiting the w2dynamics DMFT package [62, 63], a specific workflow was adopted (on the basis of that introduced in [54]):

As a first step, starting from the non-interacting case (i.e., $\Sigma(i\nu) = 0$) or from an already converged result with a similar temperature/density, we perform a DMFT calculation with a fixed density and at least 20 DMFT iterations.

As a next step, we estimate the value of the chemical potential μ so that the corresponding impurity filling coincides with the chosen density up to a precision of $5 \cdot 10^{-5}$. With the evaluated μ an other 10 DMFT loops are performed. This estimation is applied until the desired accuracy is achieved.

In the following step, a two-particle calculation is performed, computing the two-particle Green's function, and from that the on-site generalized susceptibility of the auxiliary AIM with the chemical potential previously estimated. The number of Matsubara frequencies ν and ν' used was set to 460×460 for inverse temperatures of $\beta \leq 120$, and increased to 700×700 for lower temperatures.

By inverting the Bethe-Salpeter equation for the impurity site, now, we can calculate the irreducible local vertex function in the magnetic sector ($\Gamma_m^{\nu\nu'}$), in addition to the DMFT self-energy. Now, $\chi_m(\mathbf{q})$ can be computed via the the Dyson Eq. (3.6) and the Bethe-Salpeter equations of DMFT Eq. (3.14), along a path (π, π, q_z).

This step of the calculation is repeated for different Matsubara- frequency box sizes. By means of an extrapolation to a box of infinite size, the the maximum value $\chi_m(\mathbf{q})$ can be determined, e.g. fitting the frequency-box-size dependent susceptibility over the inverse of the maximal frequency of the box, using a liner fitting function.

At the same time the correlation length can be extracted by fitting the maximum-peak of $\chi_m(\mathbf{q})$ along a small interval along the q_z-direction with the Ornstein-Zernike expression (3.12) for the different frequency box sizes and, again, by carefully extrapolating the fitted values obtained up to infinite frequency box sizes.

In this procedure we resolved the maximum-peak of $\chi_m(\mathbf{q})$ in a range of $q_z = \bar{q}_z \pm 0.02$ (in unit of unitary lattice spacing, $a \equiv 1$) by approximately 40 data points. While the fitting routine is not particularly sensitive on the amount of data points, the choice of the above-mentioned q_z-range is an essential parameter, being directly related to the applicability of the Ornstein-Zernike fit, especially for low temperatures. Moreover, similarly as in RPA, the number of k-points used in

the internal summations is, obviously important in DMFT too. However, due to the presence of an imaginary part in the DMFT self-energy, the procedure requires fewer k-points compared to RPA. In particular, by employing the Gaussian quadrature method [67], we were able to reduce the required k-points to 50^3 for the lowest temperatures considered.

Chapter 4

Numerical Results

"Today is the opportunity to build the tomorrow you want."

—*Ken Poirot*

In this chapter, we present the numerical results of this work. Specifically, we analyze the properties of magnetic quantum criticality in bulk metallic systems using dynamical and static mean-field (i.e., DMFT and RPA) computations for lattices featuring lines of Kohn points or isolated Kohn points. The former scenario is demonstrated through calculations on the Hubbard model on a simple cubic lattice with nearest neighbor hopping, while the latter is illustrated using the Hubbard model with a frustrated cubic lattice.

4.1 DMFT and RPA Results

4.1.1 Hubbard Model on a Simple Cubic Lattice

In order to describe magnetic quantum phase transitions in bulk correlated metals, whose Fermi surface is characterized by the presence of lines of Kohn points, we considered the Hubbard model on a simple cubic lattice (see Eq. (2.10) in section 2.3.1.) The specific parameters chosen for our analysis were $t = 1$ for the hopping term and $U = 9.789t$ for the interaction term. This interaction strength corresponds to an intermediate to large value, for which the critical temperature T_c is maximal at half filling in DMFT [38, 45, 68]. To investigate the different regimes of the magnetic transitions, we analyzed the phase diagram as a function of temperature (T) and electronic density (n).

The main results of our DMFT calculations are shown in Fig. 4.1, where the inverse of the static magnetic susceptibility χ_m^{-1} and the inverse of the corresponding magnetic correlation length ξ_m^{-1} are displayed for four different values of the electronic density n. The maximum of χ_m^{-1} is reached at an incommensurate momentum $\mathbf{q}_{\max}(T) = (\pi, \pi, q_z = \bar{q_z} = \pi - \delta(T))$ cf. also [54], and the corresponding correlation length was extracted by fitting the behaviour of χ_m^{-1} around the maximum with the Ornstein-Zernike expression Eq. (3.12) shown in the previous chapter along

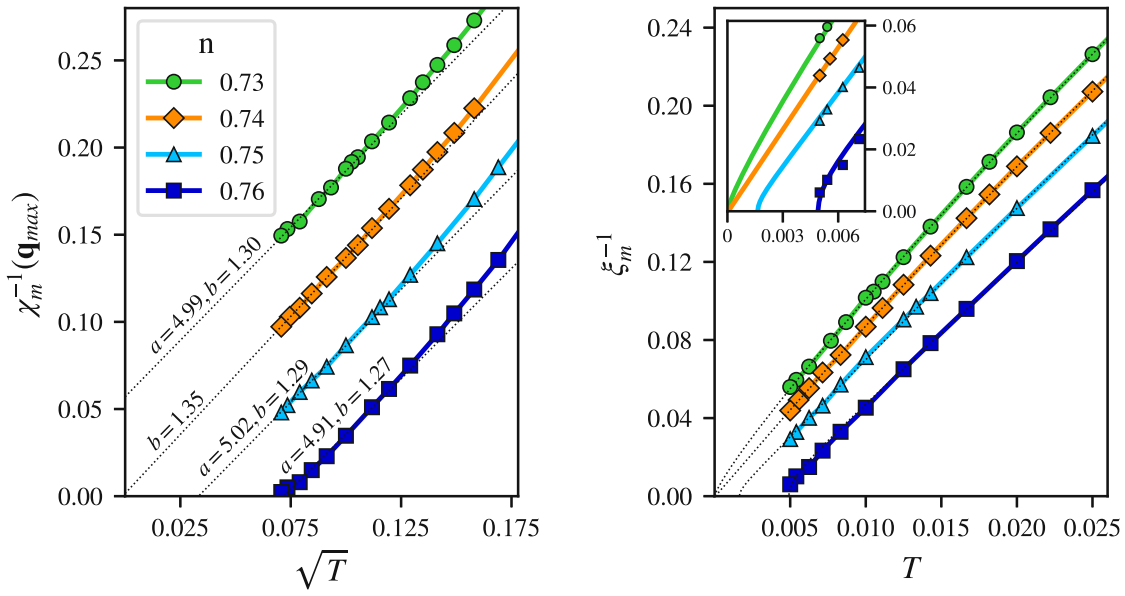

Figure 4.1: Inverse of the maximal magnetic susceptibility (left panel, cf. also the related data in [54, 69]), and the corresponding magnetic correlation length (right panel) of the DMFT solution of the 3D Hubbard model on a simple cubic lattice, plotted respectively as a function of $\sqrt{T}$ and T for four different values of the electronic density n. While the fitting parameters of χ_m^{-1} are reported in the plots, a low-T zoom of the fits of ξ_m^{-1} is shown in the inset.

the path of (π, π, q_z). The x-axis of the two panels in Fig. 4.1 , respectively $\sqrt{T}$ and T, have been chosen to highlight the most relevant trends of the physical quantities considered.

Let us start by analyzing the data for χ_m^{-1} shown in the left panel of Fig. 4.1, confirming the corresponding DMFT results presented in [54]. The maximum values of the inverse magnetic susceptibility are displayed for the densities $n = 0.73, 0.74, 0.75$ and 0.76, as well as for different temperatures with a lowest inverse temperature of $\beta = \frac{1}{T} = 200$ (with $k_B = 1$, and we also recall here that all energy units in this thesis are expressed, unless differently explicitly specified, in the units of the nearest neighboring hopping term $t = 1$). The parameters were chosen, so that our DMFT calculations were performed around the quantum critical region. Here, χ_m^{-1} scales with the square root of temperature $\chi_m^{-1} \propto \sqrt{T}$, which is clearly visible through the linear behaviour of all data w.r.t. the $\sqrt{T}$ abscissa axis. As for the the non-thermal behaviour of χ_m^{-1}, i.e. $\chi_m^{-1}(T \to 0)$, as a function of the doping n, the equal spacing between the four chosen densities, which differ one w.r.t. the others always by the same amount ($\Delta n = 0.01$), evidently indicates a *linear* scaling of $\chi_m^{-1}(T \to 0)$ w.r.t. $n_c - n$. Hence, as already noted in [54, 69], the overall behaviour of the χ_m^{-1} dataset in the left panel of Fig. 4.1 is extremely well captured by the following transparent expression:

$$\chi_m^{-1}(\mathbf{q}_{\max}(T), n, T) \simeq a(n_c - n) + b\sqrt{T}, \tag{4.1}$$

where a, b are positive constants and n_c characterizes the density where the QCP appears (at $T = 0$). In the left panel of Fig. 4.1, the χ_m^{-1} data are fitted using Eq. (4.1), and the fitting parameters are displayed in the plot. The agreement of the numerical results with the proposed function in the low-T region of our interest is evident even at a quick glance. Quantitatively, its validity is also supported by the consistency in the values of a and b in the density interval considered. Further, at the doping level of $n = 0.74$ we can trace the line of χ_m^{-1} down to $T = 0$, approaching a value very close to zero for the inverse susceptibility. A divergence in χ_m at zero temperature can be associated with the QCP of the incommensurate antiferromagnetic to paramagnetic phase transition. Extrapolating from our four different doping levels n, we estimate a critical doping of $n_c \simeq 0.74$.[1]

In the right panel of Fig. 4.1 the inverse magnetic correlation length ξ_m^{-1} is computed for the same densities and temperatures chosen for the susceptibility in the left panel. For temperatures, accessible to our DMFT calculations linear scaling in T could be supposed at a first, rough glance. However, in contrast to the case of the susceptibility, for the correlation length the spacing between the lines of different data sets is not equal, indicating no obvious n-dependence. Actually one might have supposed, that, *mutatis mutandis* an "analogous" relation to Eq. (4.1) could hold for the correlation length, such as:

$$\xi_m^{-1}(n, T) \simeq \tilde{a}\sqrt{(n_c - n)} + \tilde{b}T, \tag{4.2}$$

where the (mean-field) square root behavior as a function of the density dependence would have been expected around such a magnetic QCP, associated with an effective dimensionality of $d_{\text{eff}} \equiv d + z = 3 + z > 4$, z (here supposedly larger than 1) being the dynamical critical exponent and d the space dimensionality. However, the equation Eq. (4.1.1) does *not* accurately describe the numerical data, especially close to the classical phase transition, where deviations becomes more evident. In the next chapter, we will derive that the proper functional form of the magnetic correlation length should be given by:

$$\xi_m^{-1}(T) = \sqrt{\mathcal{A}(T)\left[a(n_c - n) + b\sqrt{T}\right]}, \tag{4.3}$$

which is already exploited here to fit the data in the right panel of Fig. 4.1. The results of the fits are also displayed in the corresponding inset for the very low temperature regime, where direct numerical DMFT calculations are no longer feasible. Remarkably, the additional temperature-dependent parameter $\mathcal{A}(T)$, which controls the weight is of the Ornstein-Zernike (OZ) peak of $\chi_m(\mathbf{q})$, assumed in our fitting procedure for ξ_m, is found to be *vanishing* as $T^{\frac{3}{2}}$. As we will discuss more extensively in the next chapter, this directly reflects the breakdown of the OZ assumption

[1] We note here that the linear interpolation of $\chi_m^{-1}(T \to 0)$ obtained by fitting the data sets to the other three densities after assuming $n_c = 0.74$ yields the numerically perfectly consistent estimate of $n_c^{\text{est}} \cong 0.741$.

in the ground state. At the same time, the vanishing of $\mathcal{A}(T)$ for $T \to 0$ has crucial influence on the correlation length of the ground state. In particular, one finds that $\xi_m(T \to 0)$ diverges for all $n \leq n_c$ with $\xi_m^{-1}(T) \propto T^{\frac{3}{4}}$ for $n \leq n_c$, while at the critical doping ($n = n_c$), the vanishing of the first term in the square brackets of Eq. (4.3) features a perfect *linear* temperature behaviour of $\xi_m^{-1}(T)$ in the whole low-T regime. Evidently, this yields an unitary value for the corresponding quantum critical exponent $\nu = 1$.

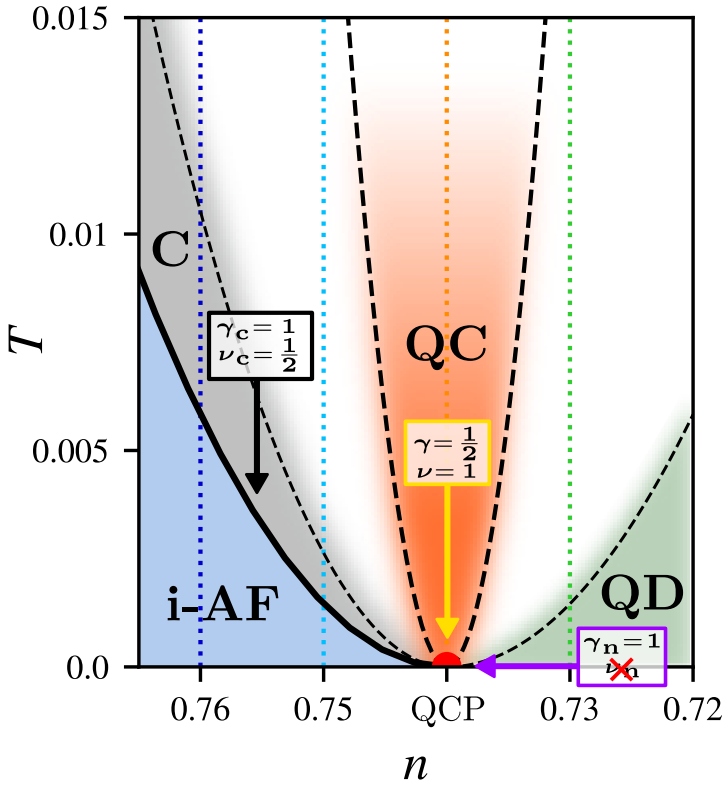

Figure 4.2: $T - n$ phase diagram of the DMFT solution of the 3D Hubbard model on a simple cubic lattice (cf. also results in [54, 69]). The quantum critical region is indicated in orange, with the funnel ending at the quantum critical point (QCP) at $T = 0$, where the incommensurate antiferromagnetic (AF) phase (blue) and the quantum disordered phase (green) are separated. The grey-shadowed area marks the classical regime close to the phase transition to the incommensurate AF (i-AF). The four dotted lines correspond to the calculations shown in Fig. 4.1. The corresponding (quantum) critical exponents are indicated in the corresponding coloured boxes.

Now we are in a good position to describe the whole phase-diagram around our magnetic QCP, following essentially the procedure presented in [54, 69]. At finite temperature a simultaneous divergence in χ_m^{-1} and ξ_m^{-1} characterizes a second order phase transition. Hence, in our case, the classical phase transition can easily be identified by following the fitted lines in Fig. 4.1 down to χ_m^{-1} or $\xi_m^{-1} = 0$, a condition, which determines the critical temperature T_c for any values of $n > n_c$. Furthermore, one can set criteria [54, 69] for identifying the quantum critical region "QC" (which will be defined as the regime, where the temperature-dependent term in Eq. (4.1) dominates over the non-thermal, density dependent term) and the quantum disordered region

"QD" (where, instead, the doping-dependent non-thermal term will be the dominant one), with a crossover region between the two regimes.

Additionally, in the parameter region above the line characterizing the classical phase transition at T_c, our expressions Eq. (4.1) [54] and Eq. (4.3) can be Taylor expanded w.r.t. $(T - T_c)$. Then, the dominating leading-order term directly corresponds to classical critical mean-field exponent values for both χ_m^{-1} [54] and ξ_m^{-1} as actually expected at finite T in DMFT, see Sec. 5.1.
It is important to note here that, due to their intrinsic crossover nature, the precise location of the borders delimiting the quantum critical and quantum disordered regions will quantitatively depend on the chosen criteria. In our analysis [69], we chose following conditions on Eq. (4.1) resulting in a phase diagram shown in Fig. 4.2:

- Classical region ("C"): first order term in the Taylor expansion of Eq. (4.1) as large as second order term in Eq. (5.5)
- Quantum-critical region ("QC"): temperature dependent term $b\sqrt{T}$ five times as large as doping dependent term $a(n - n_c)$
- Quantum disordered region ("QD"): temperature dependent term $b\sqrt{T}$ as large as large as doping dependent term $a(n - n_c)$

In Fig. 4.2 the quantum critical region is highlighted in orange, the classical region in gray, the quantum disordered region in green and the incommensurate antiferromagnetic region in blue. White spaces indicate crossover regions related to the criteria stated above. The four dotted lines correspond to the calculations shown in Fig. 4.1. Additionally the thermal, non-thermal and classical critical exponents are displayed. Notably, as also discussed in [54], the shape of the quantum critical funnel, as well as all other crossover transition lines, are *quadratic* in the $T-n$ phase diagram, at odds with many well-known cases (e.g. see Fig. 1.4).

The results discussed above, in part first presented in [54], demonstrate how Kohn anomalies on the Fermi surface are directly reflected not only in the values of the quantum critical exponents, but also in the whole shape of the phase diagram around the magnetic QCP. Evidently, the non analytical behaviour associated to the Kohn features on the Fermi surface, which are directly encoded in the bubble term of DMFT, are preserved by the DMFT Bethe-Salpeter equation BSE Eq. (3.14) due to the purely local nature of its irreducible vertex.

Let us now compare the results presented above for DMFT with the RPA calculations, which were conducted at the lower interaction strength of $U = 3.02$. This choice of U allows to obtain a similar critical density n_c in RPA and DMFT. Given the significantly lower numerical complexity of RPA compared to DMFT, we have been able to enhance the resolution of the calculations of our key quantities. This improvement has then allowed us, to more easily extend our analysis to lattices with different Fermi surface geometries.

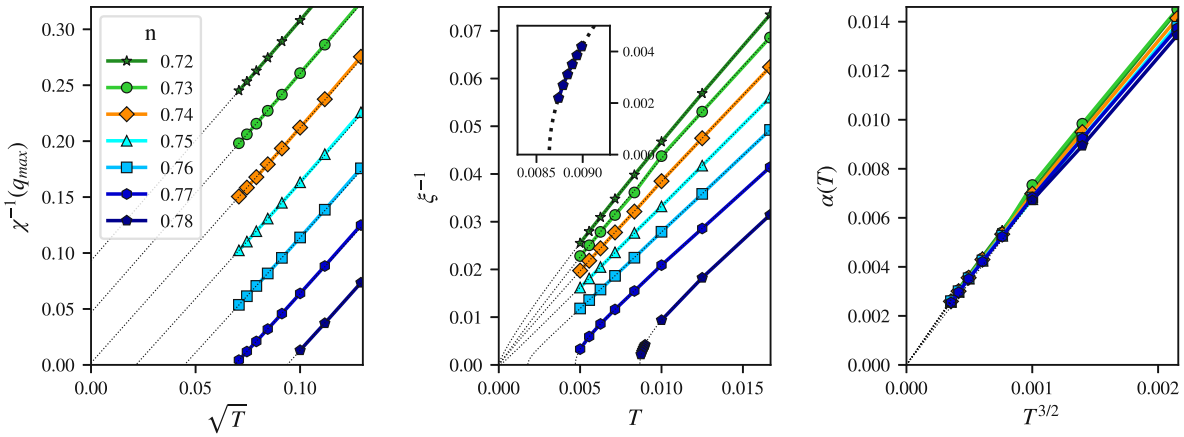

Figure 4.3: Inverse of the maximal magnetic susceptibility (left), the corresponding magnetic correlation length (middle), and the Ornstein-Zernike fitting parameter $\mathcal{A}(T)$ (right) of the RPA solution of the 3D Hubbard model with a simple cubic lattice, plotted respectively as a function of $\sqrt{T}$, T, and $T^{\frac{3}{2}}$ for different values of the electronic density n.

In Fig. 4.3, we plot the inverse magnetic susceptibility χ_m^{-1} and the inverse correlation length ξ_m^{-1} as functions of $\sqrt{T}$ and T, respectively. In the inset of the middle panel, data for ξ_m^{-1} at a density of $n = 0.78$ is displayed, highlighting the behavior in the immediate vicinity of the phase transition. Additionally, the Ornstein-Zernike fitting parameter $\mathcal{A}(T)$ is displayed in the right panel of Fig. 4.3, showing the $T^{\frac{3}{2}}$ behavior mentioned earlier. Evidently, the qualitative agreement between the results from RPA and DMFT is quite robust. Parallel and equally spaced lines of χ_m^{-1} in the left panel of Fig. 4.3 indicate the stated relation for χ_m^{-1} in Eq. (4.1) showing an overall alignment of the RPA computations with the trends of the DMFT data displayed in Fig. 4.1. Moreover, the results for ξ_m^{-1} well match the functional form in Eq. (4.3) in both RPA and DMFT.

4.1.2 Hubbard Model on a Frustrated Cubic Lattice

Having started with the simple cubic lattice, where lines of Kohn points appear on the Fermi surface [42, 45, 64], the second case we want to analyze is quantum criticality for lattices exhibiting *isolated* Kohn points on their Fermi surface. As discussed in Chap. 2 adding frustration to the simple cubic lattice can change the Fermi geometry surface in the desired way with Kohn points appearing as isolated features on the Fermi surface [42]. To get a quick insight in this second case, we can proceed as follows. Having established a clear qualitative correspondence of between DMFT and RPA calculations for the behavior of the susceptibility and of the correlation length around the magnetic QCP of the simple cubic system, we choose now the RPA method to get a first, but already reliable picture of the corresponding (quantum) critical properties for systems with qualitatively different Fermi surface geometries.

In order to tune the critical density of the quantum phase-transition to a similar value ($n_c \simeq 0.74$) as in the previous case, here we set the next-nearest-neighbor hopping $t' = 0.2t$ and the interaction

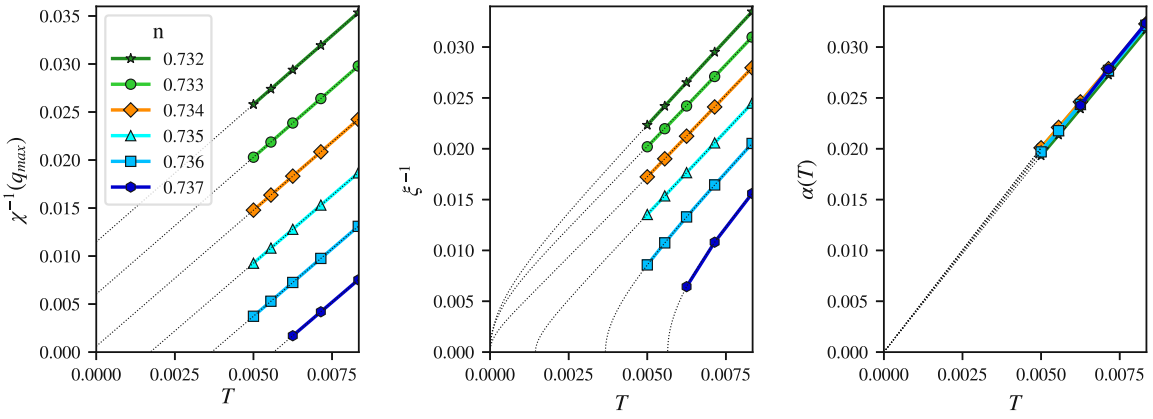

Figure 4.4: Inverse of the maximal magnetic susceptibility (left), the corresponding magnetic correlation length (middle), and the Ornstein-Zernike fitting parameter $\mathcal{A}(T)$ (right) of the RPA solution of the 3D Hubbard model with a frustrated cubic lattice with $t' = 0.2t$. All three quantities are plotted as functions of T and are displayed for different values of the electronic density n.

strength to $U = 4$. In Fig. 4.4, we plotted the inverse magnetic susceptibility χ_m^{-1}, correlation length ξ_m^{-1}, and the Ornstein-Zernike (OZ) fitting parameter $\mathcal{A}(T)$, all as functions of temperature T.

While the behavior of the correlation length in the quantum critical region $\xi_m^{-1} \propto T^\nu$ (with $\nu = 1$) remains essentially unchanged compared to the simple cubic lattice with Kohn lines, the plot of χ_m^{-1} is markedly different. All lines in Fig. 4.4 display linearity w.r.t. the $T-$axis, indicating a functional form as:

$$\chi_m^{-1}(\mathbf{q}_{\max}, n, T) \simeq a(n_c - n) + b\,T, \tag{4.4}$$

which evidently corresponds to a quantum critical exponent of $\gamma = 1$, instead of the exponent $\gamma = \frac{1}{2}$ in Eq. (4.1). From the susceptibility data at any finite T we can again extract the correlation length, yielding:

$$\xi_m^{-1}(T) = \sqrt{\mathcal{A}(T)\,[a(n_c - n) + b\,T]}. \tag{4.5}$$

The Ornstein-Zernike weight now scales as $\mathcal{A}(T) \propto T$, as it is clearly shown in the right panel of Fig. 4.4 by linearity in the chosen scaling of the x-axis. Inserting $\mathcal{A}(T)$ into Eq. (4.5) allows us recover the temperature scaling $\xi_m^{-1} \propto T$ in the quantum critical region stated above.

At the same time, in the quantum disordered region for $n < n_c$, in spite of a finite $\xi_m^{-1}(T \to 0)$, the extrapolated $T \to 0$ value of $\xi_m^{-1}(T)$ displays a clear $\sqrt{T}$ dependence in the zero T-limit

(analogous, but not identical to the $T^{\frac{3}{2}}$ of the Kohn line case). This behavior, as we will discuss in the next chapter, signals the breakdown of the Ornstein Zernike relation in the ground state.

Another notable difference between lattices with Kohn lines and isolated Kohn points is the overall shape of the phase diagram around the QCP. In fact, as illustrated in the previous section, from $\chi_m^{-1}(T)$ we can also extract the critical temperature as well as the crossover borders of the quantum critical and classical regions. Summarizing our observations for the phase diagrams in Fig. 4.5 (cf. [54, 69]), we see that in contrast to the quadratic shape in Fig. 4.2, the presence of isolated Kohn points results in a linearly shaped transition and crossover lines.

Eventually, as we will also discuss with more details in the next chapter, in a "standard" case of 3D systems, whose FS does not display any Kohn anomaly, the conventional low-T Sommerfeld behavior of the magnetic susceptibility will feature DMFT/RPA quantum critical exponents equal to $\gamma = 2$ and $\nu = 1$. This will be then reflected (cf. [54, 69]) in a much more conventional square-root-like behaviour of all crossover/transition lines around the magnetic QCP.

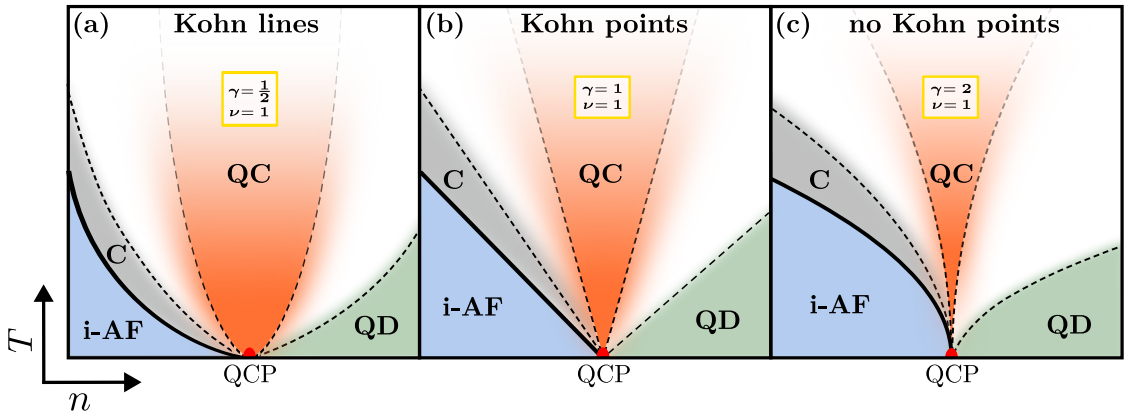

Figure 4.5: Schematic DMFT phase diagrams for 3D systems, whose FS displays (a) Kohn lines (e.g., simple cubic lattice), (b) isolated Kohn points (e.g., frustrated cubic or FCC lattice [42, 64]), or (c) no Kohn point at all (standard case, e.g. BCC [42]). The quantum critical funnels with different shapes are displayed in orange, the quantum disordered region in blue, and the incommensurate antiferromagnetic (i-AF) phase in green. The gray shaded area indicates the classical critical region associated to the finite T transition. The plot is re-adapted from [54]

.

Chapter 5

Empirical and Analytical Analysis

"E quando ci fermiamo sulla riva lo sguardo all'orizzonte se ne va
portandoci i pensieri alla deriva per quell'idea di troppa libertà"

—*Umberto Tozzi*

In this chapter, we aim to rationalize the qualitative pictures established via the DMFT and RPA calculations presented in the previous chapter. First, we will empirically summarize the quantum critical features for lattices with different kind of Kohn anomalies on the Fermi-surfaces and compare them to the standard case without Kohn anomalies. Then, we will derive analytical expressions for the susceptibility and correlation length at the RPA level, linking our findings to the numerical data presented in Chap. 4.

5.1 Empirical Descriptions of Quantum Criticality in the Presence of Kohn Anomalies

We start by considering the non-interacting case ($U = 0$). In general, when computing the corresponding bubble susceptibility χ_0^{-1} for a 3D system, one gets a functional form which reads:

$$\chi_0^{-1} = A(n) + B(T, n), \tag{5.1}$$

with an explicitly temperature dependent B, whose behavior is controlled by the Fermi surface geometry and, unless in special cases, can be assumed weakly density dependent. At the same time, the functional form of χ_0^{-1} exhibits a density dependent term $A(n) \geq 0$, which entails the $T = 0$ properties. The next step is, then, to apply the RPA:

$$\chi_{m,\mathrm{RPA}}^{-1} = \chi_0^{-1} - U \implies \chi_{m,\mathrm{RPA}}^{-1} = [A(n) - U] + B(T). \tag{5.2}$$

Evidently, if $A(n) = U$ the the first term will vanish. This can be associated with a quantum phase-transition occurring at the (quantum) critical density value of $n = n_c$. Hence, by encoding the change of the sign of $A(n)-U$ in the spirit of Landau theory, one would write it as $a(n_c-n)$. In this way, we recover a non-thermal quantum critical scaling for the magnetic susceptibility, which perfectly matches the functional behavior observed in Fig. 4.1, Fig. 4.3 and Fig. 4.4, independent of the geometry of the Fermi surface. As we will explicitly discuss, the different behaviour of the latter term $B(T)$, instead, strongly affects the thermal quantum critical exponents.

5.1.1 Fermi Surfaces with Lines of Kohn Points

Let us start by considering the case, where the Fermi surface displays lines of Kohn points, whose numerical results have been shown in 4.1.1. In this case the $B(T)$ term displays a square root low-T behavior, and, hence, the inverse magnetic susceptibility exhibits the functional form

$$\chi_m^{-1}(n,T) = a(n_c - n) + b\sqrt{T} \qquad a, b > 0. \tag{5.3}$$

The corresponding critical temperature T_c of the magnetic transition is then directly defined through the divergence of χ_m (and, simultaneously, of ξ_m) at

$$\chi_m^{-1}(T_c) = 0 \implies T_c = \frac{a^2(n_c - n)^2}{b^2}, \tag{5.4}$$

which is perfectly consistent with the numerical data reported in Fig. 4.2. At the same time, in the vicinity of a classical phase transition, the classical critical behavior must be observed. Specifically, in DMFT/RPA this should correspond to the mean-field universality class ($\gamma_{\rm cl} = 1, \nu_{\rm cl} = \frac{1}{2}$). While, at a first glance, the "universal" $\sqrt{T}$-behavior of Eq. (5.3) might seem incompatible with a classical mean-field criticality, one can then see that our expectation is actually fulfilled, by expanding the susceptibility around $T \approx T_c$. In fact, since the expression for χ_m^{-1} in Eq. (5.3) is analytical for all $T > 0$, by Taylor expanding χ_m^{-1} at $T \simeq T_c$, we readily recover the corresponding mean-field exponent (highlighted in gray in the following section):

$$\chi_m^{-1}(T \approx T_c) \cong A(T - T_N)^{\gamma_{\rm cl}=1} + B(T - T_N)^2 + \dots \qquad T > T_c. \tag{5.5}$$

At the same time, it is clear that, in the parameter region of the $T - n$ phase-diagram *exactly* above the QCP the vanishing of the "mass term" $n_c - n$ in Eq. (5.3) makes no longer possible a Taylor expansion around $T_c = 0$ and, then, one has:

$$\chi_m^{-1}(T = T_c = 0) \propto T^{\gamma=0.5} \qquad \text{for} \quad n = n_c. \tag{5.6}$$

This yields the quite different value ($\gamma = \frac{1}{2}$) for the quantum critical exponent (highlighted in red) w.r.t. the mean-field value $\gamma_{cl} = 1$, as well as w.r.t. the prediction of the HMM theory ($\gamma = \frac{3}{2}$).

Further, as discussed in previous chapters, the Ornstein-Zernike formula directly relates χ_m and ξ_m through a temperature-dependent parameter $\mathcal{A}(T)$, which describes the weight of the peak of the magnetic susceptibility in momentum space. Specifically, for an incommensurate antiferromagnetic instability the q_z-dependence of χ_m around $(\pi, \pi, \bar{q}_z)$=$(\pi, \pi, \pi - \delta(T)$ can be well captured by

$$\chi_m(q_z, T) = \frac{\mathcal{A}(T)}{(q_z - \bar{q}_z)^2 + \xi_m^{-2} + \mathcal{C}(q_z - \bar{q}_z)^3} = \left.\frac{\mathcal{A}(T)}{\xi_m^{-2}}\right|_{q_z = \bar{q}_z}. \tag{5.7}$$

Hence, at the maximum of χ_m (i.e. for $q_z = \bar{q}_z(T)$), we are left with a conveniently simple relation between the susceptibility and the correlation length. Then, by evaluating Eq. (5.7) at $q_z = \bar{q}_z$ and inserting Eq. (5.3), we obtain an expression for the correlation length that only depends on $\mathcal{A}(T)$ and $\chi_m(n, T)$:

$$\xi_m^{-2}(T) = \mathcal{A}(T)\chi_m^{-1}(T) = \mathcal{A}(T)\left[a(n_c - n) + b\sqrt{T}\right]. \tag{5.8}$$

In the quantum critical regime, where the temperature-dependent term of χ_m^{-1} dominates (region with doping close to the critical value), we can extract the corresponding quantum critical exponent ν, if we exploit our (numerical) observation of a low-T scaling of the coefficient $\mathcal{A}(T)$ as $\mathcal{A}(T) \propto T^{\frac{3}{2}}$, cf. right panel of Fig. 4.3. The corresponding low-T behavior of the (inverse) magnetic correlation length then reads:

$$\xi_m^{-1}(T) \propto T^{\nu=1}. \tag{5.9}$$

Moreover, we observe that for $n > n_c$, if the (positive) temperature and (negative) doping-dependent terms cancel each other out at a given temperature, the correlation length diverges there, leading exactly to the same criterion for the critical temperature as for the susceptibility in Eq. (5.4). In this case, we can simply repeat the procedure of Taylor expanding all the temperature dependent expressions in the vicinity of T_c. Inserting the expanded χ_m from Eq. (5.5) leads to the mean-field (MF) exponent for ξ_m:

$$\xi_m^{-1}(T \approx T_c) \approx \sqrt{\mathcal{A}(T)(T - T_c)} \propto (T - T_c)^{\nu_{\mathrm{cl}}=0.5} \qquad T > T_c. \tag{5.10}$$

Another way to examine this feature would be to insert the temperature scaling of χ_m and ξ_m into Eq. (5.7). Evidently, this procedure yields the exponent of $\mathcal{A}(T)$ once again, allowing to better

highlight the link among the temperature behaviours of the three quantities involved, namely $\mathcal{A}$, χ_m and ξ_m:, thorough a single expression:

$$\mathcal{A}(T) = \frac{\xi_m^{-2}(T)}{\chi_m^{-1}(T)} \propto \frac{T^{2\nu}}{T^{\gamma}} = T^{3/2}. \tag{5.11}$$

From this equation, it is evident how the vanishing behaviour of $\mathcal{A}(T)$, which corresponds to the breakdown of the Ornstein-Zernike expression in the ground states controls the magnitude of possible violations of the Fisher relation ($\gamma = 2\nu$ for $\eta = 0$).

Additionally, we want to investigate the non-thermal quantum critical exponents (outlined in green. From Eq. (5.3), we immediately see that:

$$\chi_m^{-1}(n, T = 0) = a(n_c - n)^{\gamma_n = 1}, \tag{5.12}$$

which corresponds to the exponent obtained in the conventional/HMM-theory for $d_{\text{eff}} > d + z = 4$ and indicates that Kohn points do not affect the critical behaviour in the quantum disordered region ($n < n_c$). While, as we mentioned in the first section of the present Chapter, this result holds independently of the FS geometry, it is very important to emphasize, that the same does *not* apply to the non-thermal critical behavior of the magnetic correlation length. In fact, for ξ_m it is *not* possible to define a non-thermal quantum critical exponent in the QD region, since, according to Eq. (5.10), one finds that $\mathcal{A}(T) \propto T^{\frac{3}{2}}$. Hence, $\xi_m^{-1}(T) \simeq T^{\frac{3}{4}}$ is diverging at $T \to 0$ not only at the QCP, but for *all* $n < n_c$. We associate this feature with a *breakdown* of the Ornstein-Zernike behavior, which will be discussed later in more detail.

5.1.2 Fermi Surfaces with Isolated Kohn Points

The combination of analytical and numerical analyses has provided us with a comprehensive understanding of how the presence of Kohn lines on the Fermi surface influences the magnetic quantum criticality in three dimensional electronic systems. In this section, we will apply the same procedure to two other cases of Fermi surface geometries. We will start with lattices whose Fermi surface possess isolated Kohn points and then conclude with the "standard" case of lattices where no Kohn points can be found on the Fermi surface. While part of the analytical derivations, which are fundamental for our analysis, was detailed in [45], here we will sketch the most important findings and connect them to the numerical results obtained at the level of RPA.

For the case of isolated Kohn points in a frustrated cubic lattice (see Fig. 4.3), we have evidently observed that χ_m^{-1} scales linearly with temperature, in contrast to the square root dependence on T observed in the previous case with Kohn lines:

$$\chi_m^{-1}(T) = a(n_c - n) + bT \qquad a, b > 0. \tag{5.13}$$

The scaling w.r.t. the doping n, however, is not affected by the details of the FS geometry and still exhibits a linear form. When computing the critical temperature in the T–n phase diagram, a *linearly* shaped critical temperature T_c:

$$\chi_m^{-1}(T_c) = 0 \implies T_c = \frac{a(n - n_c)}{b}. \tag{5.14}$$

For similar reasons as in the Kohn line case, the linearity of Eq. (5.13) also shapes the crossover borders around the QCP in the T–n phase diagram, namely the quantum critical funnel as well as the border of the quantum disordered region. As for the classical exponent, the Taylor expansion around T_c is here straightforward because the overall linear behavior of χ_m^{-1} in Eq. (5.13) directly yields the mean-field critical exponent:

$$\chi_m^{-1}(T \approx T_c) \cong A(T - T_c)^{\gamma_{cl}=1} \qquad T > T_c. \tag{5.15}$$

At the same, it also affects [45, 64], more remarkably, the corresponding thermal quantum critical exponent:

$$\chi_m^{-1}(T = T_c = 0) \propto T^{\gamma=1}. \tag{5.16}$$

As for the critical exponent ν: Let us consider once again the Ornstein-Zernike relation, used to fit the correlation length from the susceptibility distribution:

$$\chi_m(q_z, T) = \frac{\mathcal{A}(T)}{(q_z - \bar{q}_z)^2 + \xi_m^{-2} + \mathcal{C}(q_z - \bar{q}_z)^3} = \left.\frac{\mathcal{A}(T)}{\xi_m^{-2}}\right|_{q_z = \bar{q}_z}, \tag{5.17}$$

where after setting $q_z = \bar{q}_z$, we insert Eq. (5.13) we get:

$$\xi_m^{-2}(T) = \mathcal{A}(T)\,[\,a(n_c - n) + bT\,]. \tag{5.18}$$

Our numerical observations in the previous sections clearly indicates that $\mathcal{A}(T) \propto T$. Hence, in the vicinity of the critical doping, where the mass term becomes negligible, the inverse correlation length will read:

$$\xi_m^{-1}(T) \propto T^{\nu=1} \tag{5.19}$$

Therefore, in contrast to the susceptibility and the corresponding quantum critical exponent γ, the exponent ν, describing how the correlation length scales, remains *unchanged*, compared to the case with Kohn lines. Similarly, also the classical critical exponent stays unchanged:

$$\xi_m^{-1}(T \approx T_c) \approx \sqrt{\mathcal{A}(T_c)(T - T_c)} \propto (T - T_c)^{\nu_{cl}=0.5} \qquad T > T_c. \tag{5.20}$$

Repeating the same analysis as for the Kohn line case, we note that the knowledge of the quantum critical exponents $\gamma = \nu = 1$ (and the corresponding violation of the Fisher relation) [45, 64] can be only rationalized in terms of an $\mathcal{A}(T)$, which, in this case, vanishes linearly for $T \to 0$:

$$\mathcal{A}(T) = \frac{\xi_m^{-2}(T)}{\chi_m^{-1}(T)} \propto \frac{T^{-2\nu}}{T^{-\gamma}} = T^1 \qquad \text{for } \nu = 1 = \gamma. \tag{5.21}$$

Eventually, for densities smaller than the critical density n_c, the non-thermal quantum critical exponent γ_n remains unchanged w.r.t. the previous case:

$$\chi_m^{-1}(T = 0) \approx a(n_c - n)^{\gamma_n=1} \qquad \text{for } n < n_c, \tag{5.22}$$

while the vanishing of $\mathcal{A}(T \to 0)$ and the associated breakdown of the OZ behavior, still prevents to define a corresponding quantum critical exponent for the correlation length.

In summary, the behavior of the correlation length, as well as the non-thermal scaling in n, is essentially the same[1] for quantum critical systems with isolated Kohn points and Kohn lines. The susceptibility, however, depends on the temperature in a different manner featuring a different quantum critical exponent γ. The relation between γ and ν, which violates the Fisher relation is *de facto* encoded in the T-scaling of the Ornstein-Zernike fitting parameter $\mathcal{A}(T)$.

5.1.3 Fermi Surface without Kohn Anomalies

To complete the empirical discussion on the differences in magnetic quantum criticality in lattices with different Fermi surface geometries, we discuss here a case where no Kohn points are present.

[1] To be precise, the divergence of $\xi_m(T \to 0)$ in the whole quantum disordered regime is slightly milder than in the case of Kohn lines of the FS, featuring a $T^{-\frac{1}{2}}$ instead of the previously mentioned $T^{-\frac{3}{4}}$ behavior.

Unlike the previous sections, we will go through the procedure previously followed without referring, however, to any specific numerical datasets or calculations. We will rely instead on general properties of Fermi Liquid systems. One possible (and simple) lattice geometry, to which the considerations of this section may be applicable, is the BCC lattice, where our algorithm presented in [42] did not find any Kohn points. A word of caution is however needed: The search for the nesting vector Q was made more difficult in the BCC lattice w.r.t. the simple cubic case by more complicated symmetries appearing when searching for the maxima in the three-dimensional susceptibility bubble.

For cases with no Kohn points, we expect:

$$\chi_m^{-1}(T) = -a(n_c - n) + bT^2 \qquad a, b > 0, \tag{5.23}$$

with the critical exponent $\gamma = 2$, corresponding to a *Sommerfeld*-like behavior of the susceptibility. Due to the expected a linear scaling in doping n, the corresponding critical temperature exhibits then the textbook square-root-like behavior [34, 70]:

$$\chi_m^{-1}(T_c) = 0 \implies T_c = \sqrt{\frac{a(n_c - n)}{b}}, \tag{5.24}$$

which for analogous reasons as in the other case, will also shape all the crossover borders around the QCP. Furthermore, not surprisingly, exactly as in the previous sections, we can expand around T_c, again yielding the mean-field exponent:

$$\chi_m^{-1}(T \approx T_c) \cong A(T - T_c)^{\gamma_{\text{cl}}=1} + B(T - T_c)^2 \qquad T > T_c. \tag{5.25}$$

At the same time, at quantum criticality, the mass term vanishes, leaving us with a purely quadratic function. Therefore, in the expansion, the linear term disappears, leaving the quadratic term as the lowest order:

$$\chi_m^{-1}(T = T_c = 0) \propto T^{\gamma=2}. \tag{5.26}$$

Turning now to discuss the correlation length, the corresponding Ornstein-Zernike formula reads:

$$\chi_m(q_z, T) = \frac{\mathcal{A}(T)}{(q_z - \bar{q}_z)^2 + \xi_m^{-2} + \mathcal{C}(q_z - \bar{q}_z)^3} = \left.\frac{\mathcal{A}(T)}{\xi_m^{-2}}\right|_{q_z = \bar{q}_z} \tag{5.27}$$

with

$$\xi_m^{-2}(T) = \mathcal{A}(T)\left[a(n_c - n) + bT^2\right]. \tag{5.28}$$

Differently as in the other cases, since this time no Kohn points are present, there is no reason to expect a $T = 0$ breakdown of the Ornstein-Zernike relation. Hence, we expect $\mathcal{A}(T \to 0) = \mathcal{A}_0 > 0$, yielding $\nu = 1$ from Eq. (5.28). On another perspective, if we insert the exponents $\gamma = 2$ and $\nu = 1$, which fulfill the Fisher ($\gamma = 2\nu$) one indeed gets:

$$\mathcal{A}(T) = \frac{\xi_m^{-2}(T)}{\chi_m^{-1}(T)} \propto \frac{T^{-2\nu}}{T^{-\gamma}} = \text{const.} \qquad \text{for } \gamma = 2\nu. \tag{5.29}$$

In fact, the validity of the Fisher relation implies that $\mathcal{A}(T = 0)$ should not vanish or, more physically, that the Ornstein-Zernike formulation should not break down in the zero temperature limit.

As about the classical exponent ν_{cl}, we have

$$\xi_m^{-1}(T \approx T_c) \approx \mathcal{A}(T_c)\sqrt{(T - T_c)} \propto (T - T_c)^{\nu_{\text{cl}}=0.5} \qquad T > T_c, \tag{5.30}$$

which, not surprisingly, yields once again the mean-field exponent and, similarly also the non-thermal exponent remains the same:

$$\chi_m^{-1}(0) \approx (n_c - n)^{\gamma_n=1} \qquad \text{for } n < n_c \qquad \text{with } \mathcal{A}(T = 0) = \text{const.} \tag{5.31}$$

Differently from the previous cases, however, the finiteness of $\mathcal{A}(T \to 0)$, prevents a divergence of $\xi_m(T \to 0)$ in the whole quantum disordered region. This allows, this time, to define the corresponding non-thermal quantum critical exponent ν_n. Evidently, then, the validity of the OZ relation determines the exponent to be $\nu_n = \frac{1}{2}$.

5.2 Analytical Descriptions

Hitherto, our analysis has been primarily based on numerical calculations. Now, however, we aim to approach the problem from the perspective of analytical derivations.

In the supplemental material of [45] a formula for the non-interacting susceptibility bubble of a 3D systems, whose Fermi surfaces feature lines of Kohn points, as a function of the z-component of the momentum $q_z = q_z + \vec{q}_z^{\,0}$ and the instability vector $\mathbf{q}_{max}(T = 0) = (\pi, \pi, \vec{q}_z^{\,0} = \pi - \delta(T{=}0))$

was derived and discussed extensively with $\chi_0\left((\pi,\pi,q_z=\delta q_z+\bar{q}_z^0),T\right)\equiv\chi_0(q_z,T)$:

$$\chi_0(q_z,T)=\chi_{\rm nu}^0-\frac{C_1}{T\,v}\left[(C_2T+v\,\delta q_z)^{\frac{3}{2}}\ln\frac{C_3}{C_2\,T+v\,\delta q_z}+\pi\,(C_2T-v\,\delta q_z)^{\frac{3}{2}}\right]. \tag{5.32}$$

Without delving into the details here, let us break down the components of this expression: $\chi_0^{\rm nu}$ is the non-universal contribution, which we can consider weakly dependent on momentum and temperature. The constants C_1, C_2, and C_3 include all relevant system-dependent prefactors, and v is the magnitude of the Fermi velocity. As demonstrated in the Supplemental Material of [45], this result is directly driven by the presence of Kohn points on on the Fermi Surface, as it is also highlighted by the fact that the most important geometrical features characterizing the Fermi surface ($\mathbf{q}_{max}$-vector, Fermi velocity) are explicitly present in Eq. (5.32). Note that q_z is the only relevant momentum component due to the symmetry of the simple cubic lattice, and our specific choice of $\mathbf{q}_{max}=(\pi,\pi,\pi-\delta)$.

Next, following the Supplemental material of [45] one can observe that the quantity $\delta Q_z\simeq -C_2\,T/v$ describes the shift of the position of the susceptibility peak-maximum with temperature, and $\delta\mathbf{q}_{max}(T)=\mathbf{q}_{max}(T)-\mathbf{q}_{max}(0)=(0,0,\delta Q_z)$, the difference between the thermal and non-thermal magnetic instability vector. Expanding near the temperature-dependent maximum, one obtains [45]:

$$\chi_0(q_z,T)\simeq\chi_0(\bar{q}_z,T{=}0)-BT^{1/2}-C\frac{(\delta q_z-\delta Q_z)^2}{T^{3/2}}\qquad\text{with}\,B>0,C>0. \tag{5.33}$$

with new positive constants B, and C. Recalling the RPA expression discussed in Section 3.1, we can insert the above expression for non-interacting bubble:

$$[\chi_{m,\rm RPA}(q_z,T)]^{-1}=[\chi_0(q_z,T)]^{-1}-U=\left[\chi_0(\bar{q}_z,T{=}0)-BT^{\frac{1}{2}}-C\frac{(\delta q_z-\delta Q_z)^2}{T^{\frac{3}{2}}}\right]^{-1}-U. \tag{5.34}$$

In our study of the quantum critical behavior, we are interested to evaluate Eq. (5.2) in the low-T limit and (i) either directly at $\mathbf{q}_{max}(T)\equiv\delta q_z-\delta Q_z=0$ (for the analysis of T-dependence of the maximal magnetic susceptibility) or (ii) for very small deviation w.r.t. that value. In both case, the term $BT^{\frac{1}{2}}$ is very small, while the last term in the square bracket in Eq. (5.2) is either (i) exactly 0 or also quite small (ii) due to its numerator. In any case, the following expansion holds for the term in the square brackets

$$\frac{1}{1-x}\simeq 1+x+\ldots\qquad\text{for}\,|x|<1, \tag{5.35}$$

where we set $x = BT^{\frac{1}{2}} + C\frac{(\delta q_z - \delta Q_z)^2}{T^{\frac{3}{2}}}$, yielding:

$$[\chi_{m,\mathrm{RPA}}(q_z, T)]^{-1} = [\chi_0(\bar{q}_z, T=0)]^{-1} - U + bT^{\frac{1}{2}} + c\frac{(\delta q_z - \delta Q_z)^2}{T^{\frac{3}{2}}}, \tag{5.36}$$

where $b, c > 0$, while the quantity $[\chi_0(\bar{q}_z^0, T=0)]^{-1} - U$ is no longer positive-defined, its change of sign marking the value of the critical density (n_c) of the QCP. Assuming a smooth/analytical density dependence of $[\chi_0(\bar{q}_z^0, T=0)]^{-1}$, in the spirit of the Landau theory, we can, thus, parameterize this "mass term" as: $[\chi_0(\bar{q}_z, T=0)]^{-1} - U \simeq a(n_c - n)$ with $a > 0$.

One can then immediately see how, when evaluating Eq. (5.36) at $\mathbf{q}_{max}(T)$, i.e., in our case, for $q_z = \bar{q}_z(T)$, one gets exactly the same expression as in Eq. (4.1) and Eq. (5.3): $\chi_{m,\mathrm{RPA}} \simeq a(n_c - n) + b\sqrt{T}$, and, hence, the discussed description of the quantum criticality.

If, instead, we consider the momentum dependence of in a suitable small region of q_z around $\bar{q}_z(T)$, i.e. for small values of the variable $\delta q_z - \delta Q_z$, we get:

$$\chi_{m,\mathrm{RPA}}(q_z, T) \simeq \frac{c^{-1}\, T^{\frac{3}{2}}}{[q_z - \bar{q}_z(T)]^2 + c^{-1}\, T^{\frac{3}{2}}[a(n_c - n) + b\sqrt{T}]}, \tag{5.37}$$

which obviously entails the temperature behavior of the maximal susceptibility discussed above for $q_z = \bar{q}_z(T)$, but, most remarkably, also allows us to identify the parameters of Ornstein-Zernike expression in Eq. (5.27) as:

$$c^{-1}\, T^{\frac{3}{2}} = \mathcal{A}(T), \tag{5.38}$$

$$c^{-1}\, T^{\frac{3}{2}}[a(n_c - n) + b\sqrt{T}] = \xi_m^{-2}. \tag{5.39}$$

Hence, the corresponding expression of the correlation length features a perfect agreement with our numerical observations.

$$\xi_m^{-1} \propto \sqrt{T^{\frac{3}{2}}\left[a(n_c - n) + bT^{\frac{1}{2}}\right]} \xrightarrow{T\to 0} 0 \quad \text{for} \quad n \leq n_c. \tag{5.40}$$

The direct link between Eq. (5.32), Eq. (5.36) and Eq. (5.40) rigorously demonstrates the relation between the presence lines of Kohn anomalies on a 3D Fermi surfaces, the values of the (quantum) critical exponents, the overall shape of the phase diagram around the QCP, as well as the breakdown of the Ornstein-Zernike in the ground state.

In a similar manner, we can derive expressions for the case where isolated Kohn points are present

on the Fermi surface. Beginning with Eq. (30) from the supplemental material in [45], we find that the susceptibility bubble exhibits a linear temperature dependence on T. Consequently, we also obtain $\mathcal{A}(T) \propto T$.

5.3 Summary of (Quantum) Critical Exponents

The insight gained from our results and from their interpretations allows us to recast our findings in a very general and transparent framework for the three kind of 3D electronic systems, whose Fermi surfaces (FS) display (i) Kohn lines, (ii) isolated Kohn points, or (iii) no Kohn points at all (see Fig. 4.5). In summary, the analytical derivations for the magnetic spin-susceptibility ξ_m and the corresponding correlation length ξ_m for systems exhibiting these Fermi surface geometries, yield generalized expressions:

$$\chi_m^{-1}(\mathbf{q}_{\max}, T, n) = a(n_c - n) + b\,T^g \tag{5.41}$$

and, for $n < n_c$:

$$\xi_m^{-1}(T, n) = \sqrt{T^{2-g}\,[\,a(n_c - n) + b\,T^g\,]}, \tag{5.42}$$

with $g = 1/2$ for (i), $g = 1$ for (ii), and $g = 2$ for (iii), the latter simply corresponding to the standard Sommerfeld expansion of χ_m. Hence, for the quantum critical exponents, we evidently have $\gamma = g$ and $\nu = 1$. For $n > n_c$ we can also define the corresponding critical temperature, now generalized for all cases, and obtain:

$$T_c = \left[\,\frac{a(n_c - n)}{b}\,\right]^{\frac{1}{g}}, \tag{5.43}$$

which we identify as (i) a quadratic, (ii) a linear, and (iii) a square-root-shaped behaviour, which, in fact, also applies to all crossover borders around the magnetic QCP. These results are fascinating, as they purely stem from the properties of the Fermi surface geometry, and as shown in the previous chapter, completely drive the DMFT numerical description of magnetic QCPs, as well as even part of the findings obtained in the literature beyond DMFT [45].

Chapter 6

Conclusion and Outlook

"Life is like riding a bicycle. To keep your balance you must keep moving"

—*Albert Einstein*

In this thesis, we explored the influence of Kohn anomalies of Fermi surface geometries on magnetic quantum criticality in bulk metallic systems by computing the magnetic susceptibility and the corresponding correlation length, using both static and dynamical mean-field theory (DMFT) approaches. In particular, after that recent progress has unveiled [54] the "universal" low-temperature functional form of the DMFT susceptibility around a magnetic quantum critical point, our goal was to clarify the still not understood behavior of the magnetic correlation length as well as the precise relations of the (quantum) critical exponents of the two quantities.

In three-dimensional lattices, Kohn anomalies can manifest on the Fermi surface as lines of Kohn points in highly symmetric situations, such as simple cubic lattices [42, 45], or as isolated Kohn points in geometrically frustrated lattices, such as, e.g., the frustrated cubic and the FCC lattice [42, 64]. Our combined numerical (DMFT) and semi-analytical (RPA) study of the Hubbard model on cubic lattices has not only confirmed how the Kohn anomalies shape the whole phase diagram around the magnetic quantum critical point (QCP), but has eventually clarified the underlying relation between magnetic susceptibility and corresponding correlation length in all relevant parameter regimes of the problem. In particular, we have been able to directly connect our numerical results, including the most puzzling ones for the magnetic correlation length, to the general analytical derivations for 3D systems with different kind of Kohn anomalies, presented in the Supplemental Material of [45]. This link has allowed for a rigorous explanation of the relation between the corresponding (quantum) critical exponent γ and ν in the classical critical, quantum critical and quantum disordered region of the phase diagram. Remarkably, we could trace some of the previous difficulties in interpreting the numerical results for the magnetic correlation length to the breakdown of the Ornstein-Zernike relation for the magnetic susceptibility in the zero temperature limit, which also directly reflects the presence of Kohn anomalies on the underlying Fermi surface.

While the validity of the results obtained is obviously limited by the mean-field neglect of non-local space correlations, our findings remain, nonetheless, significant for several reasons.

First of all, the higher effective dimensionality induced by the temporal quantum fluctuations is known to mitigate the effects of spatial correlations on the quantum critical behavior. In particular, as the effective dimensionality of the magnetic QCP of our interest should be higher than 4, one expects that the critical exponents of the quantum disordered regime would remain unaffected by the inclusion of spatial correlations beyond DMFT. It less clear, instead, whether the same might apply to the Kohn-dominated exponents in the quantum critical regime - a question which provides an interesting topic for future dedicated studies.

Second, the results obtained might represent a very useful "compass" for a correct interpretation of ab-initio many-body investigations of strongly correlated systems, often based on the merger of density functional theory and DMFT (DFT+DMFT [71, 72]), in the proximity of their magnetic quantum phase transitions. At the same time, the mean-field nature of our results might allow to individuate intriguing connections with pure mean-field calculations of magnetically ordered phases in two-dimensional lattice models with Kohn-anomalies of different kind on their 2D Fermi surfaces [73, 74].

Third, the rigorous description of the magnetic quantum criticality at the DMFT level will provide a solid theoretical framework for future studies of the effects of non-local spatial correlations, e.g. via diagrammatic extensions of DMFT [37], in lower dimensional or layered systems.

Finally, this thesis work has exclusively focused on the (quantum) critical properties entailed in the static ($\omega = 0$) magnetic response of the problem considered. Due to the intrinsic dynamical aspects of quantum criticality, in the future, it would be interesting to extend our investigation to the *dynamical* (i.e., $\omega \neq 0$) response of our 3D lattice systems, in order to unveil the behavior of the characteristic timescales of magnetic fluctuations and, where it applies, of the corresponding dynamical critical exponent in all relevant regions of the phase diagram around the magnetic QCP.

Bibliography

1. Nishimori, H. & Ortiz, G. Elements of Phase Transitions and Critical Phenomena (2011).
2. Ehrenfest, P. Phasenumwandlungen im ueblichen und erweiterten Sinn, classifiziert nach den entsprechenden Singularitaeten des thermodynamischen Potentiales. https://books.google.at/books?id=--RItwAACAAJ (N. V. Noord-Hollandsche Uitgevers Maatschappij, 1933).
3. Papon, P., Leblond, J. & Meijer, P. The physics of phase transitions: Concepts and applications, 1–409 (2006).
4. Papon, P., Leblond, J. & Meijer, P. The Physics of Phase Transitions: Concepts and Applications. ISBN: 9783540432364. https://books.google.at/books?id=3K7vAAAAMAAJ (Springer, 2002).
5. Stanley, H. Introduction to Phase Transitions and Critical Phenomena. ISBN: 9780195053166. https://books.google.at/books?id=C3BzcUxoaNkC (Oxford University Press, 1987).
6. Blundell, S. & Blundell, K. Concepts in Thermal Physics. ISBN: 9780199562091. https://books.google.at/books?id=T0luBAAAQBAJ (OUP Oxford, 2010).
7. Vojta, M. Thermal and Quantum Phase Transitions (lecture notes, Les Houches Doctoral Training School in Statistical Physics). 2015.
8. Löhneysen, H. v., Rosch, A., Vojta, M. & Wölfle, P. Fermi-liquid instabilities at magnetic quantum phase transitions. *Reviews of Modern Physics* **79,** 1015–1075. ISSN: 1539-0756. http://dx.doi.org/10.1103/RevModPhys.79.1015 (2007).
9. Sachdev, S. Quantum Phase Transitions 2nd ed. (Cambridge University Press, 2011).
10. Stanley, H. Introduction to Phase Transitions and Critical Phenomena. ISBN: 9780195053166. https://books.google.at/books?id=C3BzcUxoaNkC (Oxford University Press, 1987).
11. Custers, J. *et al.* The break-up of heavy electrons at a quantum critical point. *Nature* **424,** 524–527. ISSN: 1476-4687. http://dx.doi.org/10.1038/nature01774 (2003).
12. Ando, Y. *et al.* Resistive upper critical fields and irreversibility lines of optimally doped high-T_c cuprates. *Phys. Rev. B* **60,** 12475–12479. https://link.aps.org/doi/10.1103/PhysRevB.60.12475 (1999).
13. Barišić, N., Chan, M. K., Li, Y., Yu, G., Zhao, X., Dressel, M., Smontara, A. & Greven, M. Universal sheet resistance and revised phase diagram of the cuprate high-temperature superconductors. *Proceedings of the National Academy of Sciences* **110,** 12235–12240 (2013).

14. Ren, Z.-A. & Zhao, Z.-X. Research and Prospects of Iron-Based Superconductors. *Advanced Materials* **21,** 4584–4592 (2009).

15. Shibauchi, T., Carrington, A. & Matsuda, Y. A Quantum Critical Point Lying Beneath the Superconducting Dome in Iron Pnictides. *Annual Review of Condensed Matter Physics* **5,** 113–135. ISSN: 1947-5462. http://dx.doi.org/10.1146/annurev-conmatphys-031113-133921 (2014).

16. Landau, L. D. On the theory of phase transitions. *Zh. Eksp. Teor. Fiz.* **7** (ed ter Haar, D.) 19–32 (1937).

17. Cyrot, M. Ginzburg-Landau theory for superconductors. *Reports on Progress in Physics* **36,** 103. https://dx.doi.org/10.1088/0034-4885/36/2/001 (1973).

18. Goldenfeld, N. Lectures On Phase Transitions And The Renormalization Group. Publisher Copyright: © 1992 Taylor & Francis Group LLC. ISBN: 9780201554090 (Westview Press, 1992).

19. Cheung, A. Phase Transitions and Collective Phenomena (2011).

20. Stanley, H. E. Power laws and universality. *Nature* **378** (1995).

21. Hertz, J. A. Quantum critical phenomena. *Phys. Rev. B* **14,** 1165–1184. https://link.aps.org/doi/10.1103/PhysRevB.14.1165 (1976).

22. Millis, A. J. Effect of a nonzero temperature on quantum critical points in itinerant fermion systems. *Phys. Rev. B* **48,** 7183–7196. https://link.aps.org/doi/10.1103/PhysRevB.48.7183 (1993).

23. Moriya, T. & Kawabata, A. Effect of spin fluctuations on itinerant electron ferromagnetism. II. *Journal of the Physical Society of Japan* **35,** 669–676 (1973).

24. Moriya, T. & Takahashi, Y. Spin Fluctuations in Itinerant Electron Magnetism. *Journal de Physique Colloques* **39,** C6-1466–C6-1471. https://doi.org/10.1051/jphyscol:19786588 (1978).

25. Dzyaloshinskii, I. E. & Kondratenko, P. S. Theory of Weak Ferromagnetism of a Fermi Liquid. *Zh. Eksp. Teor. Fiz.* **70,** 1987–2005. https://link.springer.com/article/10.1007/BF02728686 (1976).

26. Binney, J. J., Dowrick, N. J., Fisher, A. J. & Newman, M. E. J. The Theory of critical phenomena: An Introduction to the renormalization group (Oxford Science Publications, 1992).

27. Löhneysen, H. v., Rosch, A., Vojta, M. & Wölfle, P. Fermi-liquid instabilities at magnetic quantum phase transitions. *Rev. Mod. Phys.* **79,** 1015–1075. https://link.aps.org/doi/10.1103/RevModPhys.79.1015 (2007).

28. Schäfer, T. Classical and quantum phase transitions in strongly correlated electron systems. PhD thesis (TU Wien, 2016).

29. Si, Q., Rabello, S., Ingersent, K. & Smith, J. L. Locally critical quantum phase transitions in strongly correlated metals. *Nature* **413,** 804–808. ISSN: 1476-4687. http://dx.doi.org/10.1038/35101507 (2001).

30. Coleman, P. & Schofield, A. J. Quantum criticality. *Nature* **433,** 226–229. ISSN: 1476-4687. http://dx.doi.org/10.1038/nature03279 (2005).

31. Mahan, G. D. Many Particle Physics, Third Edition (Plenum, New York, 2000).

32. Stefanucci, G. & van Leeuwen, R. Nonequilibrium Many-Body Theory of Quantum Systems: A Modern Introduction (Cambridge University Press, 2013).

33. Rammer, J. Quantum Field Theory of Non-equilibrium States (Cambridge University Press, 2007).

34. Abrikosov, A., Gorkov, L. & Dzyaloshinski, I. Methods of Quantum Field Theory in Statistical Physics. ISBN: 9780486632285. https://books.google.at/books?id=E_9NtwNY7UcC (Dover Publications, 1975).

35. Abrikosov, A. A., Dzyaloshinskii, I., Gorkov, L. P. & Silverman, R. A. Methods of quantum field theory in statistical physics. https://cds.cern.ch/record/107441 (Dover, New York, NY, 1975).

36. Rohringer, G., Valli, A. & Toschi, A. Local electronic correlation at the two-particle level. *Phys. Rev. B* **86,** 125114. https://link.aps.org/doi/10.1103/PhysRevB.86.125114 (2012).

37. Rohringer, G. *et al.* Diagrammatic routes to nonlocal correlations beyond dynamical mean field theory. *Rev. Mod. Phys.* **90,** 025003. https://link.aps.org/doi/10.1103/RevModPhys.90.025003 (2018).

38. Rohringer, G. New routes towards a theoretical treatment of nonlocal electronic correlations. PhD thesis (TU Wien, 2013).

39. Chalupa-Gantner, P. The nonperturbative feats of local electronic correlation: The physics of irreducible vertex divergences. PhD thesis (TU Wien, 2022).

40. Reitner, M. Generalized Susceptibilities of the Anderson Impurity Model: Fingerprints of Local Moment Physics and Kondo Screening at the Two-Particle Level. 2019.

41. Bickers, N. Self-Consistent Many Body Theory for Condensed Matter Systems, 237–296 (Springer New York, 2004).

42. Fus, D. R. Visualization of Fermi surface Kohn-anomalies in three dimensions. 2024.

43. Kohn, W. Image of the Fermi Surface in the Vibration Spectrum of a Metal. *Phys. Rev. Lett.* **2,** 393–394. https://link.aps.org/doi/10.1103/PhysRevLett.2.393 (1959).

44. Kohn, W. & Luttinger, J. M. New Mechanism for Superconductivity. *Phys. Rev. Lett.* **15,** 524–526. https://link.aps.org/doi/10.1103/PhysRevLett.15.524 (1965).

45. Schäfer, T., Katanin, A. A., Held, K. & Toschi, A. Interplay of Correlations and Kohn Anomalies in Three Dimensions: Quantum Criticality with a Twist. *Phys. Rev. Lett.* **119,** 046402. https://link.aps.org/doi/10.1103/PhysRevLett.119.046402 (2017).

46. Fus, D. R. Breakdown of the many-electron perturbation expansion beyond particle-hole symmetry: An atomic limit study. 2022.

47. Rohringer, G. *et al.* Diagrammatic routes to nonlocal correlations beyond dynamical mean field theory. *Rev. Mod. Phys.* **90,** 025003 (2018).

48. Schäfer, T., Ciuchi, S., Wallerberger, M., Thunström, P., Gunnarsson, O., Sangiovanni, G., Rohringer, G. & Toschi, A. Nonperturbative landscape of the Mott-Hubbard transition: Multiple divergence lines around the critical endpoint. *Phys. Rev. B* **94,** 235108 (2016).

49. Schäfer, T., Rohringer, G., Gunnarsson, O., Ciuchi, S., Sangiovanni, G. & Toschi, A. Divergent Precursors of the Mott-Hubbard Transition at the Two-Particle Level. *Phys. Rev. Lett.* **110,** 246405 (2013).

50. Ramos, P. & Martins, M. Algebraic Bethe ansatz approach for the one-dimensional Hubbard model. *Journal of Physics A: Mathematical and General* **30,** L195 (1997).

51. Georges, A., Kotliar, G., Krauth, W. & Rozenberg, M. J. Dynamical mean-field theory of strongly correlated fermion systems and the limit of infinite dimensions. *Rev. Mod. Phys.* **68,** 13–125. https://link.aps.org/doi/10.1103/RevModPhys.68.13 (1996).

52. The Hubbard model at half a century. *Nature Physics* **9,** 523–523. ISSN: 1745-2481. https://doi.org/10.1038/nphys2759 (2013).

53. Schäfer, T. *et al.* Tracking the Footprints of Spin Fluctuations: A MultiMethod, MultiMessenger Study of the Two-Dimensional Hubbard Model. *Phys. Rev. X* **11,** 011058. https://link.aps.org/doi/10.1103/PhysRevX.11.011058 (2021).

54. Adler, S. New Routes to Strong Correlations in Spin-Orbit Driven Systems. PhD thesis (TU Wien, 2024).

55. Adler, S. The effect of atomic spin-orbit coupling on DFT+DMFT calculations of LiOsO3. MA thesis (TU Wien, 2023).

56. Gull, E., Millis, A. J., Lichtenstein, A. I., Rubtsov, A. N., Troyer, M. & Werner, P. Continuous-time Monte Carlo methods for quantum impurity models. *Rev. Mod. Phys.* **83,** 349–404. https://link.aps.org/doi/10.1103/RevModPhys.83.349 (2011).

57. Caffarel, M. & Krauth, W. Exact diagonalization approach to correlated fermions in infinite dimensions: Mott transition and superconductivity. *Phys. Rev. Lett.* **72,** 1545–1548. https://link.aps.org/doi/10.1103/PhysRevLett.72.1545 (1994).

58. Capone, M., de'Medici, L. & Georges, A. Solving the dynamical mean-field theory at very low temperatures using the Lanczos exact diagonalization. *Phys. Rev. B* **76,** 245116. https://link.aps.org/doi/10.1103/PhysRevB.76.245116 (2007).

59. Weber, C., Amaricci, A., Capone, M. & Littlewood, P. B. Augmented hybrid exact-diagonalization solver for dynamical mean field theory. *Phys. Rev. B* **86,** 115136. https://link.aps.org/doi/10.1103/PhysRevB.86.115136 (2012).

60. Lu, Y., Höppner, M., Gunnarsson, O. & Haverkort, M. W. Efficient real-frequency solver for dynamical mean-field theory. *Physical Review B* **90.** ISSN: 1550-235X. http://dx.doi.org/10.1103/PhysRevB.90.085102 (2014).

61. Maier, T., Jarrell, M., Pruschke, T. & Hettler, M. H. Quantum cluster theories. *Rev. Mod. Phys.* **77,** 1027–1080. https://link.aps.org/doi/10.1103/RevModPhys.77.1027 (2005).

62. Wallerberger, M., Hausoel, A., Gunacker, P., Kowalski, A., Parragh, N., Goth, F., Held, K. & Sangiovanni, G. w2dynamics: Local one- and two-particle quantities from dynamical mean field theory. *Computer Physics Communications* **235,** 388–399. ISSN: 0010-4655. https://www.sciencedirect.com/science/article/pii/S0010465518303217 (2019).

63. Kowalski, A., Hausoel, A., Wallerberger, M., Gunacker, P. & Sangiovanni, G. State and superstate sampling in hybridization-expansion continuous-time quantum Monte Carlo. *Phys. Rev. B* **99,** 155112. https://link.aps.org/doi/10.1103/PhysRevB.99.155112 (2019).

64. Stepanenko, A. A., Volkova, D. O., Igoshev, P. A. & Katanin, A. A. Kohn anomalies in momentum dependence of magnetic susceptibility of some three-dimensional systems. *Journal of Experimental and Theoretical Physics* **125,** 879–889. ISSN: 1090-6509. http://dx.doi.org/10.1134/S1063776117110139 (2017).

65. Rohringer, G., Valli, A. & Toschi, A. Local electronic correlation at the two-particle level. *Phys. Rev. B* **86,** 125114 (2012).

66. Del Re, L. & Toschi, A. Dynamical vertex approximation for many-electron systems with spontaneously broken SU(2) symmetry. *Phys. Rev. B* **104,** 085120. https://link.aps.org/doi/10.1103/PhysRevB.104.085120 (2021).

67. Kovvali, N. Theory and Applications of Gaussian Quadrature Methods. ISBN: 9781608457533. https://books.google.at/books?id=uTCdW8L6i8sC (Morgan & Claypool, 2011).

68. Rohringer, G. *et al.* Diagrammatic routes to nonlocal correlations beyond dynamical mean field theory. *Rev. Mod. Phys.* **90,** 025003. https://link.aps.org/doi/10.1103/RevModPhys.90.025003 (2018).

69. Adler*, S., Fus*, D., Malcolms, M., Vock, A., Held, K., Katanin, A. A., Schäfer, T. & Toschi, A. Magnetic quantum criticality: The dynamical mean-field perspective. *(in preperation)* (2024).

70. Ashcroft, N. & Mermin, N. Solid State Physics (Saunders College Publishing, Fort Worth, 1976).

71. Held, K. Electronic structure calculations using dynamical mean field theory. *Advances in Physics* **56,** 829–926. https://doi.org/10.1080/00018730701619647 (2007).

72. Kotliar, G., Savrasov, S. Y., Haule, K., Oudovenko, V. S., Parcollet, O. & Marianetti, C. A. Electronic structure calculations with dynamical mean-field theory. *Rev. Mod. Phys.* **78,** 865–951. https://link.aps.org/doi/10.1103/RevModPhys.78.865 (2006).

73. Scholle, R., Bonetti, P. M., Vilardi, D. & Metzner, W. Comprehensive mean-field analysis of magnetic and charge orders in the two-dimensional Hubbard model. *Phys. Rev. B* **108,** 035139. https://link.aps.org/doi/10.1103/PhysRevB.108.035139 (2023).

74. Scholle, R., Metzner, W., Vilardi, D. & Bonetti, P. M. Spiral to stripe transition in the two-dimensional Hubbard model. *Phys. Rev. B* **109,** 235149. https://link.aps.org/doi/10.1103/PhysRevB.109.235149 (2024).

---

* These authors contributed equally to this work.